

A BAYESIAN APPROACH FOR INFERRING NEURONAL CONNECTIVITY FROM CALCIUM FLUORESCENT IMAGING DATA

BY YURIY MISHCHENCKO*, JOSHUA T. VOGELSTEIN†, AND LIAM PANINSKI*

COLUMBIA UNIVERSITY, JOHNS HOPKINS UNIVERSITY, AND COLUMBIA UNIVERSITY

Deducing the structure of neural circuits is one of the central problems of modern neuroscience. Recently-introduced calcium fluorescent imaging methods permit experimentalists to observe network activity in large populations of neurons, but these techniques provide only indirect observations of neural spike trains, with limited time resolution and signal quality. In this work, we present a Bayesian approach for inferring neural circuitry given this type of imaging data. We model the network activity in terms of a collection of coupled hidden Markov chains, with each chain corresponding to a single neuron in the network and the coupling between the chains reflecting the network’s connectivity matrix. We derive a Monte Carlo Expectation-Maximization algorithm for fitting the model parameters; to obtain the sufficient statistics in a computationally-efficient manner, we introduce a specialized blockwise-Gibbs algorithm for sampling from the joint activity of all observed neurons given the observed fluorescence data. We perform large-scale simulations of randomly connected neuronal networks with biophysically realistic parameters and find that the proposed methods can accurately infer the connectivity in these networks given reasonable experimental and computational constraints. In addition, the estimation accuracy may be improved significantly by incorporating prior knowledge about the sparseness of connectivity in the network, via standard L_1 penalization methods.

1. Introduction. Since Ramon y Cajal discovered that the brain is a rich and dense network of neurons (Ramon y Cajal, 1904; Ramon y Cajal, 1923), neuroscientists have been intensely curious about the details of these networks, which are believed to be the biological substrate for memory, cognition, and perception. While we have learned a great deal in the last century about “macro-circuits” (the connectivity between coarsely-defined brain areas), a number of key questions remain open about “micro-circuit” structure, [that is](#), the connectivity within populations of neurons at a fine-grained cellular level. Two complementary strategies for investigating micro-circuits have been pursued extensively. *Anatomical* approaches to inferring circuitry do not rely on observing neural activity; some recent exciting examples include array tomography (Micheva and Smith, 2007), genetic “rainbow” approaches (Livet et al., 2007), and serial electron microscopy (Briggman and Denk, 2006). Our work, on the other hand, takes a *functional* approach: our aim is to infer micro-circuits by observing the simultaneous activity of a population of neurons, without making direct use of fine-grained anatomical measurements.

Experimental tools that enable simultaneous observations of the activity of many neurons are now widely available. While arrays of extracellular electrodes have been exploited for this

*

†

Keywords and phrases: Sequential Monte Carlo, Metropolis-Hastings, Spike train data, Point process, Generalized linear model

purpose (Hatsopoulos et al., 1998; Harris et al., 2003; Stein et al., 2004; Santhanam et al., 2006; Luczak et al., 2007), the arrays most often used *in vivo* are inadequate for inferring monosynaptic connectivity in large populations of neurons, as the inter-electrode spacing is typically too large to record from closely neighboring neurons¹; importantly, neighboring neurons are more likely connected to one another than distant neurons (Abeles, 1991; Braitenberg and Schuz, 1998). Alternately, calcium-sensitive fluorescent indicators allow us to observe the spiking activity of on the order of 10^3 neighboring neurons (Tsien, 1989; Yuste et al., 2006; Cossart et al., 2003; Ohki et al., 2005) within a micro-circuit. Some organic dyes achieve sufficiently high signal-to-noise ratios (SNR) that individual action potentials (spikes) may be resolved (Yuste et al., 2006), and bulk-loading techniques enable experimentalists to simultaneously fill populations of neurons with such dyes (Stosiek et al., 2003). In addition, genetically encoded calcium indicators are under rapid development in a number of groups, and are approaching SNR levels of nearly single spike accuracy as well (Wallace et al., 2008). Microscopy technologies for collecting fluorescence signals are also rapidly developing. Cooled CCDs for wide-field imaging (either epifluorescence or confocal) now achieve a quantum efficiency of $\approx 90\%$ with frame rates up to 60 Hz or greater, depending on the field of view (Djurisic et al., 2004). For *in vivo* work, 2-photon laser scanning microscopy can achieve similar frame rates, using either acoustic-optical deflectors to focus light at arbitrary locations in three-dimensional space (Iyer et al., 2006; Salome et al., 2006; Reddy et al., 2008) or resonant scanners (Nguyen et al., 2001). Together, these experimental tools can provide movies of calcium fluorescence transients from large networks of neurons with adequate SNR, at imaging frequencies of 30 Hz or greater, in both *in vitro* and *in vivo* preparations.

Given these experimental advances in functional neural imaging, our goal is to develop efficient computational and statistical methods to exploit this data for the analysis of neural connectivity; see Figure 1 for a schematic overview. One major challenge here is that calcium transients due to action potentials provide indirect observations, and decay about an order of magnitude slower than the time course of the underlying neural activity (Yuste et al., 2006; Roxin et al., 2008). Thus, to properly analyze the network connectivity, we must incorporate methods for effectively deconvolving the observed noisy fluorescence signal to obtain estimates of the underlying spiking rates (Yaksi and Friedrich, 2006; Greenberg et al., 2008; Vogelstein et al., 2009). To this end, we introduce a coupled Markovian state-space model that relates the observed variables (fluorescence traces from the neurons in the microscope’s field of view) to the hidden variables of interest (the spike trains and intracellular calcium concentrations of these neurons), as governed by a set of biophysical parameters including the network connectivity matrix. As discussed in (Vogelstein et al., 2009), this parametric approach effectively introduces a number of constraints on the hidden variables, leading to significantly better performance than standard blind deconvolution approaches. Given this state-space model, we derive a Monte Carlo Expectation Maximization algorithm for obtaining the maximum a posteriori estimates of the parameters of interest. Standard sampling procedures (e.g., Gibbs sampling or sequential Monte Carlo) are inadequate in this setting, due to the high dimensionality and ~~nonlinear~~ ~~non-linear~~, non-Gaussian dynamics of the hidden variables; we therefore develop a specialized blockwise-Gibbs approach for efficiently computing the sufficient statistics. This strategy enables us to accurately infer the connectivity matrix

¹It is worth noting, however, that multielectrode arrays which have been recently developed for use in the retina (Segev et al., 2004; Litke et al., 2004; Petrusca et al., 2007; Pillow et al., 2008) or in cell culture (Lei et al., 2008) are capable of much denser sampling.

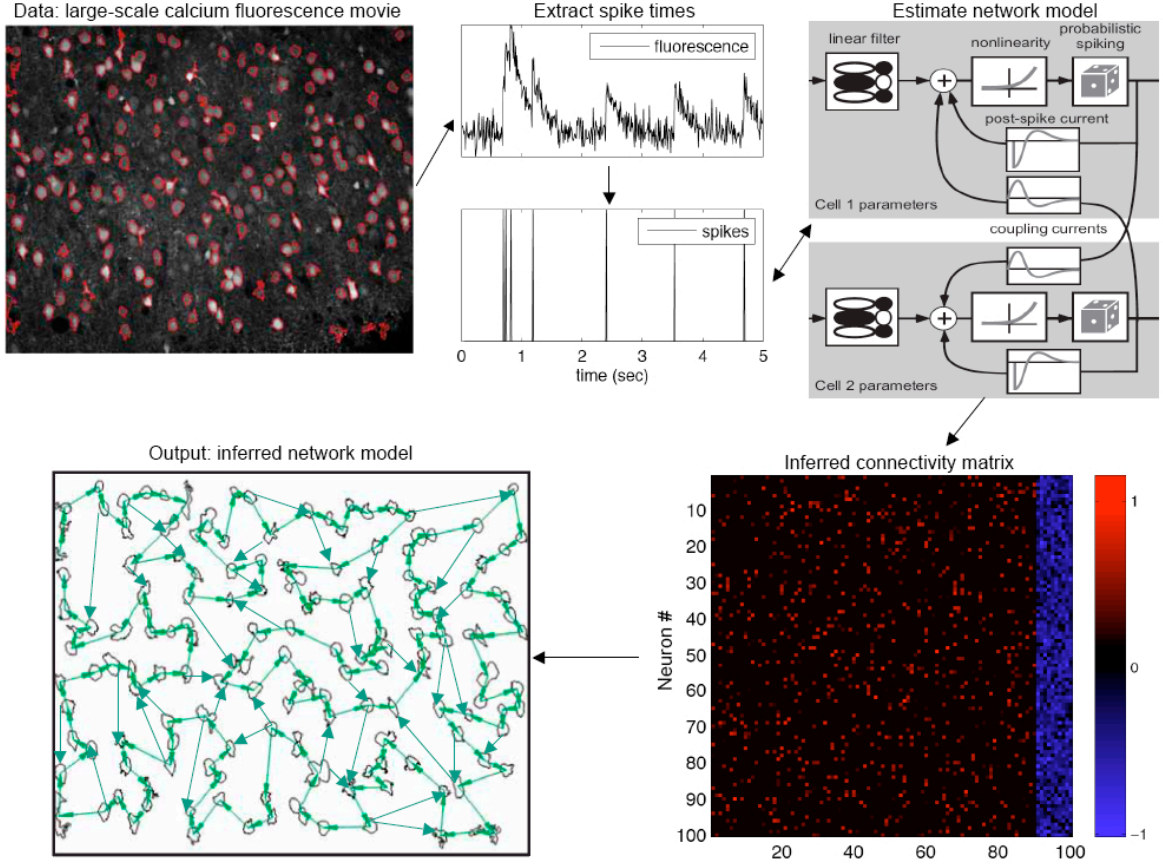


FIG 1. *Schematic overview. The raw observed data is a large-scale calcium fluorescence movie, which is pre-processed to correct for movement artifacts and find regions-of-interest, that is i.e., putative neurons. [Note that we have omitted details of these important preprocessing steps in this paper; see, for example e.g., (Cossart et al., 2003; Dombek et al., 2007) for further details.] Given the fluorescence traces $F_i(t)$ from each neuron, we estimate the underlying spike trains (i.e., the time series of neural activity) using statistical deconvolution methods. Then we estimate the parameters of a network model given the observed data. Our major goal is to obtain an accurate estimate of the network connectivity matrix, which summarizes the information we are able to infer about the local neuronal microcircuit. (We emphasize that this illustration is strictly schematic, and does not correspond directly to any of the results described below.) This figure adapted from personal communications with R. Yuste, B. Watson, and A. Packer.*

from large simulated neural populations, under realistic assumptions about the dynamics and observation parameters.

2. Methods.

2.1. Model. We begin by detailing a parametric generative model for the (unobserved) joint spike trains of all N observable neurons, along with the observed calcium fluorescence data. Each neuron is modeled as a generalized linear model (GLM). This class of models is known to capture the statistical firing properties of individual neurons fairly accurately (Brillinger, 1988; Chornoboy et al., 1988; Brillinger, 1992; Plesser and Gerstner, 2000; Paninski et al., 2004; Paninski, 2004; Rigat et al., 2006; Truccolo et al., 2005; Nykamp, 2007; Kulkarni and Paninski, 2007; Pillow et al., 2008; Vidne et al., 2009; Stevenson et al., 2009). We denote

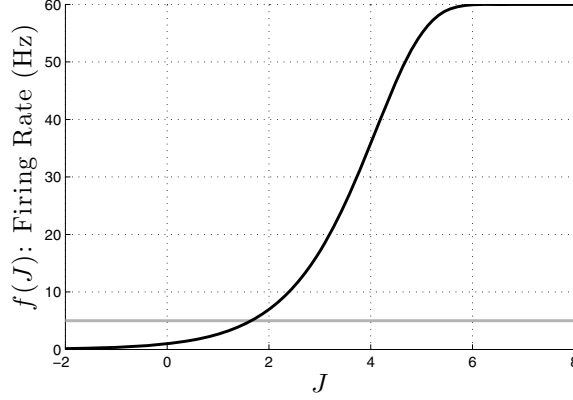


FIG 2. A plot of the firing rate nonlinearity $f(J)$ used in our simulations. Note that the firing rate saturates at $1/\Delta$, because of our Bernoulli assumption (i.e., the spike count per bin is at most one). Here the binwidth $\Delta = (60 \text{ Hz})^{-1}$. The horizontal gray line indicates 5 Hz, the baseline firing rate for most of the simulations discussed in the Results section.

the ~~ith~~ ~~th~~ neuron's activity at time t as $n_i(t)$: in continuous time, $n_i(t)$ could be modeled as an unmarked point process, but we will take a discrete-time approach here, with each $n_i(t)$ taken to be a binary random variable. We model the spiking probability of neuron i via an instantaneous nonlinear function, $f(\cdot)$, of the filtered and summed input to that neuron at that time, $J_i(t)$. This input is composed of [the following](#): (i) some baseline value, b_i ; (ii) some external vector stimulus, $S^{ext}(t)$, that is linearly filtered by k_i ; and (iii) spike history terms, $h_{ij}(t)$, encoding the influence on neuron i from neuron j , weighted by w_{ij} :

$$(1) \quad n_i(t) \sim \text{Bernoulli}[f(J_i(t))], \quad J_i(t) = b_i + k_i \cdot S^{ext}(t) + \sum_{j=1}^N w_{ij} h_{ij}(t).$$

To ensure computational tractability of the parameter inference problem, we must impose some reasonable constraints on the instantaneous nonlinearity $f(\cdot)$ (which plays the role of the inverse of the link function in the standard GLM setting) and on the dynamics of the spike-history effects $h_{ij}(t)$. First, we restrict our attention to functions $f(\cdot)$ which ensure the concavity of the spiking loglikelihood in this model (Paninski, 2004; Escola and Paninski, 2008), as we will discuss at more length below. In this paper ~~we~~ we use

$$(2) \quad f(J) = P[n > 0 \mid n \sim \text{Pois}(e^J \Delta)] = 1 - \exp[-e^J \Delta]$$

(Figure 2), where the inclusion of Δ , the time step size, ensures that the firing rate scales properly with respect to the time discretization; see (Escola and Paninski, 2008) for a proof that this $f(\cdot)$ satisfies the required concavity constraints. However, we should note that in our experience the results depend only weakly on the details of $f(\cdot)$ within the class of log-concave models (Li and Duan, 1989; Paninski, 2004) (see also section 3.4 below).

Second, because the algorithms we develop below assume Markovian dynamics, we model the spike history terms as autoregressive processes driven by the spike train $n_j(t)$:

$$(3) \quad h_{ij}(t) = (1 - \Delta/\tau_{ij}^h) h_{ij}(t - \Delta) + n_j(t - \Delta) + \sigma_{ij}^h \sqrt{\Delta} \epsilon_{ij}^h(t),$$

where τ_{ij}^h is a decay time constant, σ_{ij}^h is a standard deviation parameter, $\sqrt{\Delta}$ ensures that the statistics of this Markov process have a proper Ornstein-Uhlenbeck limit as $\Delta \rightarrow 0$, and

throughout this paper, ϵ denotes an independent standard normal random variable. Note that this model generalizes ~~(via a simple augmentation of the state variable $h_{ij}(t)$)~~ to allow each neuron pair to have several spike history terms, each with a unique time constant, which when weighted and summed allow us to model a wide variety of possible post-synaptic effects, including bursting, facilitating, and depressing synapses; see (Vogelstein et al., 2009) for further details. We restrict our attention to the case of a single time constant τ_{ij}^h per synapse here, so the deterministic part of $h_{ij}(t)$ is a simple exponentially-filtered version of the spike train $n_j(t)$. Furthermore, we assume that τ_{ij}^h is the same for all neurons and all synapses, although, in principle, ~~in principle~~ each synapse could be modeled with its unique τ_{ij}^h . We do that both for simplicity and also because we find that the detailed shape of the coupling terms $h_{ij}(t)$ had a limited effect on the inference of the connectivity matrix, as illustrated in Figure 12 below. Thus, we treat τ_{ij}^h and σ_{ij}^h as known synaptic parameters which are the same for each neuron pair (i, j) , and denote them as τ_h and σ_h hereafter. We chose values for τ_h and σ_h in our inference based on experimental data (Lefort et al., 2009); see Table 1 below. Therefore, our unknown spiking parameters are $\{\mathbf{w}_i, k_i, b_i\}_{i \leq N}$, with $\mathbf{w}_i = (w_{i1}, \dots, w_{iN})$.

The problem of estimating the connectivity parameters $\mathbf{w} = \{\mathbf{w}_i\}_{i \leq N}$ in this type of GLM, given a fully-observed ensemble of neural spike trains $\{n_i(t)\}_{i \leq N}$, has recently received a great deal of attention; see the references above for a partial list. In the calcium fluorescent imaging setting, however, we do not directly observe spike trains; $\{n_i(t)\}_{i \leq N}$ must be considered a hidden variable here. Instead, each spike in a given neuron leads to a rapid increase in the intracellular calcium concentration, which then decays slowly due to various cellular buffering and extrusion mechanisms. We in turn make only noisy, indirect, and subsampled observations of this intracellular calcium concentration, via fluorescent imaging techniques (Yuste et al., 2006). To perform statistical inference in this setting, (Vogelstein et al., 2009) proposed a simple conditional first-order hidden Markov model (HMM) for the intracellular calcium concentration $C_i(t)$ in cell i at time t , along with the observed fluorescence, $F_i(t)$:

$$(4) \quad C_i(t) = C_i(t - \Delta) + \left(C_i^b - C_i(t - \Delta) \right) \Delta / \tau_i^c + A_i n_i(t) + \sigma_i^c \sqrt{\Delta} \epsilon_i^c(t),$$

$$(5) \quad F_i(t) = \alpha_i S(C_i(t)) + \beta_i + \sqrt{(\sigma_i^F)^2 + \gamma_i S(C_i(t))} \epsilon_i^F(t).$$

This model can be interpreted as a simple driven autoregressive process: under nonspiking conditions, $C_i(t)$ fluctuates around the baseline level of C_i^b , driven by normally-distributed noise $\epsilon_i^c(t)$ with standard deviation $\sigma_i^c \sqrt{\Delta}$. Whenever the neuron fires a spike, $n_i(t) = 1$, the calcium variable $C_i(t)$ jumps by a fixed amount A_i , and subsequently decays with time constant τ_i^c . The fluorescence signal $F_i(t)$ corresponds to the count of photons collected at the detector per neuron per imaging frame. This photon count may be modeled with normal statistics, with the mean given by a saturating Hill-type function $S(C) = C/(C + K_d)$ (Yasuda et al., 2004) and the variance scaling with the mean; see (Vogelstein et al., 2009) for further discussion. Because the parameter K_d effectively acts as a simple scale factor, and is a property of the fluorescent indicator, we assume throughout this work that it is known. Figure 3 shows a couple examples depicting the relationship between spike trains and observations. It will be useful to define an effective SNR as

$$(6) \quad \text{eSNR} = \frac{E[F_i(t) - F_i(t - \Delta) \mid n_i(t) = 1]}{E[(F_i(t) - F_i(t - \Delta))^2 / 2 \mid n_i(t) = 0]^{1/2}},$$

that is, the size of a spike-driven fluorescence jump divided by a rough measure of the

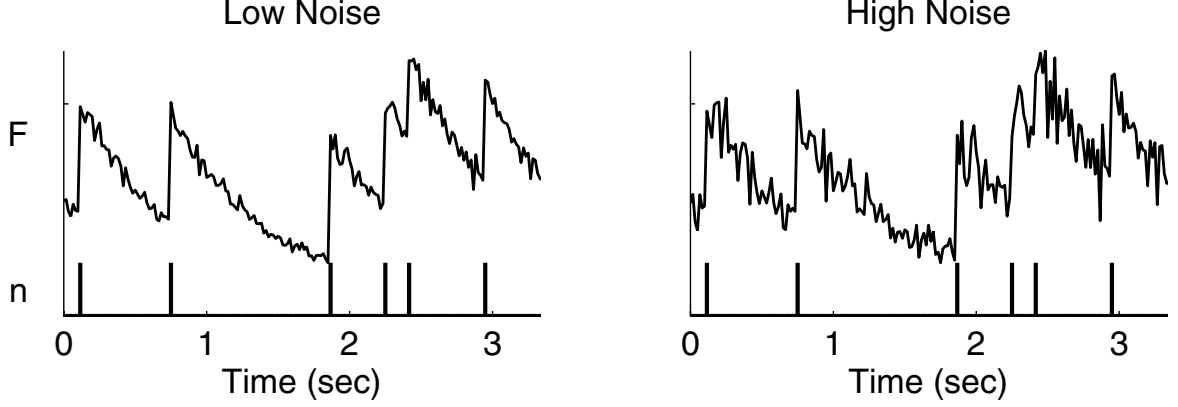


FIG 3. Two example traces of simulated fluorescence data, at different SNR levels, demonstrating the relationship between spike trains and observed fluorescence in our model. Note that both panels have the same underlying spike train. Simulation parameters: $k_i = 0.7$, $C_i^b = 1 \mu M$, $\tau_i^c = 500 \text{ msec}$, $A_i = 50 \mu M$, $\sigma_i^c = 0.1 \mu M$, $\gamma_i = 0.004$ (effective SNR ≈ 9 , as defined in Eq. (6); see also Figure 9 below) in the left panel and $\gamma_i = 0.016$ (eSNR ≈ 3) in the right panel, and $\sigma_i^F = 0$, $\Delta = (60 \text{ Hz})^{-1}$.

standard deviation of the baseline fluorescence. For concreteness, the effective SNR values in Figure 3 were 9 and 3 in the left and right panels, respectively.

To summarize, Equations (1-5) define a coupled HMM: the underlying spike trains $\{n_i(t)\}_{i \leq N}$ and spike history terms $\{h_{ij}(t)\}_{i,j \leq N}$ evolve in a Markovian manner given the stimulus $S^{ext}(t)$. These spike trains in turn drive the intracellular calcium concentrations $\{C_i(t)\}_{i \leq N}$, which are themselves Markovian, but evolving at a slower timescale τ_i^c . Finally, we observe only the fluorescence signals $\{F_i(t)\}_{i \leq N}$, which are related in a simple Markovian fashion to the calcium variables $\{C_i(t)\}_{i \leq N}$.

2.2. Goal and general strategy. Our primary goal is to estimate the connectivity matrix, \mathbf{w} , given the observed set of calcium fluorescence signals $\mathbf{F} = \{\mathbf{F}_i\}_{i \leq N}$, where $\mathbf{F}_i = \{F_i(t)\}_{t \leq T}$. We must also deal with a number of intrinsic parameters², θ_i : the intrinsic spiking parameters³ $\{b_i, w_{ii}\}_{i \leq N}$, the calcium parameters $\{C_i^b, \tau_i^c, A_i, \sigma_i^c\}_{i \leq N}$, and the observation parameters $\{\alpha_i, \beta_i, \gamma_i, \sigma_i^F\}_{i \leq N}$. We addressed the problem of estimating these intrinsic parameters in earlier work (Vogelstein et al., 2009); thus, our focus here will be on the connectivity matrix \mathbf{w} . A Bayesian approach is natural here, since we have a good deal of prior information about neural connectivity; see (Rigat et al., 2006) for a related discussion. However, a fully-Bayesian approach, in which we numerically integrate over the very high-dimensional parameter space $\theta = \{\theta_i\}_{i \leq N}$, where $\theta_i = \{\mathbf{w}_i, b_i, C_i^b, \tau_i^c, A_i, \sigma_i^c, \alpha_i, \beta_i, \gamma_i, \sigma_i^F\}$, is less attractive from a computational point of view. Thus, our compromise is to compute *maximum a posteriori* (MAP) estimates for the parameters via an expectation-maximization (EM) algorithm, in which the sufficient statistics are computed by a hybrid blockwise Gibbs sampler and sequential Monte

²The intrinsic parameters for neuron i are all its parameters minus the cross-coupling terms, that is, $\tilde{\theta}_i = \theta_i \setminus \{w_{ij}\}_{i \neq j}$.

³To reduce the notational load, we will ignore the estimation of the stimulus filter k_i below; this term may be estimated with b_i and w_{ii} using very similar convex optimization methods, as discussed in (Vogelstein et al., 2009).

Carlo (SMC) method. More specifically, we iterate the steps:

E step: Evaluate $Q(\theta, \theta^{(l)}) = E_{P[\mathbf{X}|\mathbf{F}; \theta^{(l)}]} \ln P[\mathbf{F}, \mathbf{X}|\theta] = \int P[\mathbf{X}|\mathbf{F}; \theta^{(l)}] \ln P[\mathbf{F}, \mathbf{X}|\theta] d\mathbf{X}$

M step: Solve $\theta^{(l+1)} = \underset{\theta}{\operatorname{argmax}} \left\{ Q(\theta, \theta^{(l)}) + \ln P(\theta) \right\},$

where \mathbf{X} denotes the set of all hidden variables $\{C_i(t), n_i(t), h_{ij}(t)\}_{i,j \leq N, t \leq T}$ and $P(\theta)$ denotes a (possibly improper) prior on the parameter space θ . According to standard EM theory (Dempster et al., 1977; McLachlan and Krishnan, 1996), each iteration of these two steps is guaranteed to increase the log-posterior $\ln P(\theta^{(l)}|\mathbf{F})$, and will therefore lead to at least a locally maximum a posteriori estimator.

Now, our major challenge is to evaluate the auxiliary function $Q(\theta, \theta^{(l)})$ in the E-step. Our model is a coupled HMM, as discussed in the previous section; therefore, as usual in the HMM setting (Rabiner, 1989), Q may be broken up into a sum of simpler terms:

$$\begin{aligned}
 Q(\theta, \theta^{(l)}) &= \sum_{it} \int \ln P[F_i(t)|C_i(t); \alpha_i, \beta_i, \gamma_i, \sigma_i^F] dP[C_i(t)|\mathbf{F}; \theta^{(l)}] \\
 &+ \sum_{it} \int \ln P[C_i(t)|C_i(t-\Delta), n_i(t); C_i^b, \tau_i^c, A_i, \sigma_i^c] dP[C_i(t), C_i(t-\Delta)|\mathbf{F}; \theta^{(l)}] \\
 (7) \quad &+ \sum_{it} \int \ln P[n_i(t)|\mathbf{h}_i(t); b_i, \mathbf{w}_i] dP[n_i(t), \mathbf{h}_i(t)|\mathbf{F}; \theta^{(l)}],
 \end{aligned}$$

where $\mathbf{h}_i(t) = \{h_{ij}(t)\}_{j \leq N}$. Note that each of the three sums here corresponds to a different component of the model described in [Equations Eqs. \(1-5\)](#): the first sum involves the fluorescent observation parameters, the second the calcium dynamics, and the third the spiking dynamics.

Thus, we need only compute low-dimensional marginals of the full posterior distribution $P[\mathbf{X}|\mathbf{F}; \theta]$; specifically, we need the pairwise marginals $P[C_i(t)|\mathbf{F}; \theta]$, $P[C_i(t), C_i(t-\Delta)|\mathbf{F}; \theta]$, and $P[n_i(t), \mathbf{h}_i(t)|\mathbf{F}; \theta]$. Details for calculating $P[C_i(t), C_i(t-\Delta)|\mathbf{F}_i; \tilde{\theta}_i]$ and $P[C_i(t)|\mathbf{F}_i; \tilde{\theta}_i]$ are found in (Vogelstein et al., 2009), while calculating the joint marginal for the high dimensional hidden variable \mathbf{h}_i necessitates the development of specialized blockwise Gibbs-SMC sampling methods, as we describe in the subsequent sections 2.3 and 2.4. Once we have obtained these marginals, the M-step breaks up into a number of independent optimizations that may be computed in parallel and which are therefore relatively straightforward (Section 2.5); see section 2.6 for a pseudocode summary along with some specific implementation details.

2.3. Initialization of intrinsic parameters via sequential Monte Carlo methods. We begin by constructing relatively cheap, approximate preliminary estimators for the intrinsic parameters, $\tilde{\theta}_i$. The idea is to initialize our estimator by assuming that each neuron is observed independently. Thus, we want to compute $P[C_i(t), C_i(t-\Delta)|\mathbf{F}_i; \tilde{\theta}_i]$ and $P[C_i(t)|\mathbf{F}_i; \tilde{\theta}_i]$, and solve the M-step for each $\tilde{\theta}_i$, with the connectivity matrix parameters held fixed. This single-neuron case is much simpler, and has been discussed at length in (Vogelstein et al., 2009); therefore, we only provide a brief overview here. The standard forward and backward recur-

sions provide the necessary posterior distributions, in principle (Shumway and Stoffer, 2006):

(8)

$$P[X_i(t)|F_i(0:t)] \propto P[F_i(t)|X_i(t)] \int P[X_i(t)|X_i(t-\Delta)]P[X_i(t-\Delta)|F_i(0:t-\Delta)]dX_i(t-\Delta),$$

(9)

$$P[X_i(t), X_i(t-\Delta)|\mathbf{F}_i] = P[X_i(t)|\mathbf{F}_i] \frac{P[X_i(t)|X_i(t-\Delta)]P[X_i(t-\Delta)|F_i(0:t-\Delta)]}{\int P[X_i(t)|X_i(t-\Delta)]P[X_i(t-\Delta)|F_i(0:t-\Delta)]dX_i(t-\Delta)},$$

where $F_i(s:t)$ denotes the time series \mathbf{F}_i from time points s to t , and we have dropped the conditioning on the parameters for brevity's sake. [Equation Eq. \(8\)](#) describes the forward (filter) pass of the recursion, and [Equation Eq. \(9\)](#) describes the backward (smoother) pass, providing both $P[X_i(t), X_i(t-\Delta)|\mathbf{F}_i]$ and $P[X_i(t)|\mathbf{F}_i]$ (obtained by marginalizing over $X_i(t-\Delta)$).

Because these integrals cannot be analytically evaluated for our model, we approximate them using a SMC (“marginal particle filtering”) method (Doucet et al., 2000; Doucet et al., 2001; Godsill et al., 2004). More specifically, we replace the forward distribution with a particle approximation:

$$(10) \quad P[X_i(t)|F_i(0:t)] \approx \sum_{m=1}^M p_f^{(m)}(t) \delta[X_i(t) - X_i^{(m)}(t)],$$

where $m = 1, \dots, M$ indexes the M particles in the set (M was typically set to about 50 in our experiments), $p_f^{(m)}(t)$ corresponds to the relative “forward” probability of $X_i(t) = X_i^{(m)}(t)$, and $\delta[\cdot]$ indicates a Dirac mass. Instead of using the analytic forward recursion, [Equation Eq. \(8\)](#), at each time step, we update the particle weights using the particle forward recursion

$$(11) \quad p_f^{(m)}(t) = P[F_i(t)|X_i^{(m)}(t)] \frac{P[X_i^{(m)}(t)|X_i^{(m)}(t-\Delta)]p_f^{(m)}(t-\Delta)}{q[X_i^{(m)}(t)]},$$

where $q[X_i^{(m)}(t)]$ is the proposal density from which we sample the particle positions $X_i^{(m)}(t)$. In this work, we use the “one-step-ahead” sampler (Doucet et al., 2000; Vogelstein et al., 2009), [that is](#), $q[X_i^{(m)}(t)] = P[X_i^{(m)}(t)|X_i^{(m)}(t-\Delta), F_i(t)]$. After sampling and computing the weights, we use stratified resampling (Douc et al., 2005) to ensure the particles accurately approximate the desired distribution. Once we complete the forward recursion from $t = 0, \dots, T$, we begin the [backward](#) ~~backwards~~ pass from $t = T, \dots, 0$, using

$$(12) \quad r^{(m,m')}(t, t-\Delta) = p_b^{(m)}(t) \frac{P[X_i^{(m)}(t)|X_i^{(m')}(t-\Delta)]p_f^{(m)}(t-\Delta)}{\sum_{m'} P[X_i^{(m)}(t)|X_i^{(m')}(t-\Delta)]p_f^{(m')}(t-\Delta)}$$

$$(13) \quad p_b^{(m')}(t-\Delta) = \sum_{j=1}^M r^{(m,m')}(t, t-\Delta),$$

to obtain the approximation

(14)

$$P[X_i(t), X_i(t-\Delta)|F_i] \approx \sum_{m,m'} r_i^{(m,m')}(t, t-\Delta) \delta[X_i(t) - X_i^{(m)}(t)] \delta[X_i(t-\Delta) - X_i^{(m')}(t-\Delta)];$$

for more details, see (Vogelstein et al., 2009). Thus, ~~Equations~~ [equations](#) (10-14) may be used to compute the sufficient statistics for estimating the intrinsic parameters $\tilde{\theta}_i$ for each neuron.

As discussed following [Equation](#) ~~Eq.~~ (7), the M-step decouples into three independent sub-problems. The first term depends on only $\{\alpha_i, \beta_i, \gamma_i, \sigma_i\}$; since $P[F_i(t)|S(C_i(t)); \tilde{\theta}_i]$ is Gaussian, we can estimate these parameters by solving a weighted regression problem (specifically, we use a coordinate-optimization approach: we solve a quadratic problem for $\{\alpha_i, \beta_i\}$ while holding $\{\gamma_i, \sigma_i\}$ fixed, then estimate $\{\gamma_i, \sigma_i\}$ by the usual residual error formulas while holding $\{\alpha_i, \beta_i\}$ fixed). Similarly, the second term requires us to optimize over $\{\tau_i^c, A_i, C_i^b\}$, and then we use the residuals to estimate σ_i^c . Note that all the parameters mentioned so far are constrained to be non-negative, but may be solved efficiently using standard quadratic program solvers if we use the simple reparameterization $\tau_i^c \rightarrow 1 - \Delta/\tau_i^c$. Finally, the last term may be expanded:

$$(15) \quad E[\ln P[n_i(t), \mathbf{h}_i(t)|\mathbf{F}; \theta_i]] \\ = P[n_i(t), \mathbf{h}_i(t)|\mathbf{F}; \theta_i] \ln f[J_i(t)] + (1 - P[n_i(t), \mathbf{h}_i(t)|\mathbf{F}; \theta_i]) \ln[1 - f(J_i(t))];$$

since $J_i(t)$ is a linear function of $\{b_i, \mathbf{w}_i\}$, and the right-hand side of [Equation](#) ~~Eq.~~ (15) is concave in $J_i(t)$, we see that the third term in [Equation](#) ~~Eq.~~ (7) is a sum of terms which are concave in $\{b_i, \mathbf{w}_i\}$ — and therefore also concave in the linear subspace $\{b_i, w_{ii}\}$ with $\{w_{ij}\}_{i \neq j}$ held fixed — and may thus be maximized efficiently using any convex optimization method, [for example, e.g.](#) ~~Newton-Raphson~~ [Newton-Raphson](#) or conjugate gradient ascent.

Our procedure therefore is to initialize the parameters for each neuron using some default values that we have found to be effective in practice in analyzing real data, and then iteratively (i) estimate the marginal posteriors via the SMC recursions (10-14) (E step), and (ii) maximize over the intrinsic parameters θ_i (M step), using the separable convex optimization approach described above. We iterate these two steps until the change in $\tilde{\theta}_i$ does not exceed some minimum threshold. We then use the marginal posteriors from the last iteration to seed the blockwise Gibbs sampling procedure described below for approximating $P[n_i, \mathbf{h}_i|\mathbf{F}; \theta_i]$.

2.4. Estimating joint posteriors over weakly coupled neurons. Now we turn to the key problem: constructing an estimate of the joint marginals $\{P[n_i(t), \mathbf{h}_i(t)|\mathbf{F}; \theta]\}_{i \leq N, t \leq T}$, which are the sufficient statistics for estimating the connectivity matrix \mathbf{w} [[recall Equation](#) ~~(recall Eq. (7))~~]. The SMC method described in the preceding section only provides the marginal distribution over a single neuron’s hidden variables; this method may in principle be extended to obtain the desired full posterior $P[\mathbf{X}(t), \mathbf{X}(t - \Delta)|\mathbf{F}; \theta]$, but SMC is fundamentally a sequential importance sampling method, and therefore scales poorly as the dimensionality of the hidden state $\mathbf{X}(t)$ increases (Bickel et al., 2008). Thus, [we](#) need a different approach.

One very simple idea is to use a Gibbs sampler: sample sequentially from

$$(16) \quad X_i(t) \sim P[X_i(t)|\mathbf{X}_{\setminus i}, X_i(0), \dots, X_i(t - \Delta), X_i(t + \Delta), \dots, X_i(T), \mathbf{F}; \theta],$$

looping over all cells i and all time bins t . Unfortunately, this approach is likely to mix poorly, due to the strong temporal dependence between $X_i(t)$ and $X_i(t + \Delta)$. Instead, we propose a blockwise Gibbs strategy, sampling one spike train as a block:

$$(17) \quad \mathbf{X}_i \sim P[\mathbf{X}_i|\mathbf{X}_{\setminus i}, \mathbf{F}; \theta].$$

If we can draw these blockwise samples $\mathbf{X}_i = \mathbf{X}_i(s : t)$ efficiently for a large subset of $t - s$ adjacent time-bins simultaneously, then we would expect the resulting Markov chain to

mix much more quickly than the single-element Gibbs chain. This follows due to the weak dependence between \mathbf{X}_i and \mathbf{X}_j when $i \neq j$, and the fact that Gibbs is most efficient for weakly-dependent variables (Robert and Casella, 2005).

So, how can we efficiently sample from $P[\mathbf{X}_i|\mathbf{X}_{\setminus i}, \mathbf{F}; \theta]$? One attractive approach is to try to re-purpose the SMC method described above, which is quite effective for drawing approximate samples from $P[\mathbf{X}_i|\mathbf{X}_{\setminus i}, F_i; \theta]$ for one neuron i at a time. Recall that sampling from an HMM is in principle easy by the “propagate forward, sample backward” method: we first compute the forward probabilities $P[X_i(t)|\mathbf{X}_{\setminus i}(0:t), F_i(0:t); \theta]$ recursively for timesteps $t = 0$ up to T , then sample ~~backward~~ backwards from $P[X_i(t)|\mathbf{X}_{\setminus i}(0:T), F_i(0:T), X_i(t-\Delta); \theta]$. This approach is powerful because each sample requires just linear time to compute [*i.e.*, $O(T/\Delta)$ time, where T/Δ is the number of desired time steps]. Unfortunately, in this case we can only compute the forward probabilities approximately (via Equations Eqs. 10-11), and so therefore this attractive forward-backward approach only provides approximate samples from $P[\mathbf{X}_i|\mathbf{X}_{\setminus i}, \mathbf{F}; \theta]$, not the exact samples required for the validity of the Gibbs method.

Of course, in principle, we should be able to use the Metropolis-Hastings ~~Metropolis-Hastings~~ (M-H) algorithm to correct these approximate samples. The problem is that the M-H acceptance ratio in this setting involves a high-dimensional integral over the set of paths that the particle filter might possibly trace out, and is therefore difficult to compute directly. (Andrieu et al., 2007) discuss this problem at more length, along with some proposed solutions. A slightly simpler approach was introduced by (Neal et al., 2003). Their idea is to exploit the $O(T/\Delta)$ forward-backward sampling method by embedding a discrete Markov chain within the continuous state space \mathcal{X}_t on which $X_i(t)$ is defined; the state space of this discrete embedded chain is sampled randomly according to some distribution ρ_t with support on \mathcal{X}_t . It turns out that an appropriate Markov chain (incorporating the original state space model transition and observation probabilities, along with the auxiliary sampling distributions ρ_t) may be constructed quite tractably, guaranteeing that the samples produced by this algorithm have the desired equilibrium density. See (Neal et al., 2003) for details.

We can apply this embedded-chain method directly here to sample from $P[\mathbf{X}_i|\mathbf{X}_{\setminus i}, \mathbf{F}; \theta]$. The one remaining question is how to choose the auxiliary densities ρ_t . We would like to choose these densities to be close to the desired marginal densities $P[X_i(t)|\mathbf{X}_{\setminus i}, \mathbf{F}; \theta]$, and conveniently, we have already computed a good (discrete) approximation to these densities, using the SMC methods described in the last section. The algorithm described in (Neal et al., 2003) requires the densities ρ_t to be continuous, so we simply convolve our discrete SMC-based approximation [~~specifically, the $X_i(t)$ -marginal of Equation 14~~ Eq. 14] with an appropriate normal density to arrive at a very tractable mixture-of-Gaussians representation for ρ_t .

Thus, to summarize, our procedure for approximating the desired joint state distributions $P[n_i(t), \mathbf{h}_i(t)|\mathbf{F}; \theta]$ has a Metropolis-within-blockwise-Gibbs flavor, where the internal Metropolis step is replaced by the $O(T/\Delta)$ embedded-chain method introduced by (Neal et al., 2003), and the auxiliary densities ρ_t necessary for implementing the embedded-chain sampler are obtained using the SMC methods from (Vogelstein et al., 2009).

2.4.1. A factorized approximation of the joint posteriors. If the SNR in the calcium imaging is sufficiently high, then, by definition, ~~by definition~~ the observed fluorescence data F_i will provide enough information to determine the underlying hidden variables \mathbf{X}_i . Thus, in this case the joint posterior approximately factorizes into a product of marginals for each neuron

i :

$$(18) \quad P[\mathbf{X}|\mathbf{F}; \theta] \approx \prod_{i \leq N} P[\mathbf{X}_i|\mathbf{F}; \tilde{\theta}_i].$$

We can take advantage of this because we have already estimated all the marginals on the ~~right-hand~~ ~~right-hand~~ side using the approximate SMC methods in Section 2.3. This factorized approximation entails a significant gain in efficiency for two reasons: first, it obviates the need to generate joint samples via the expensive blockwise-Gibbs approach described above; and second, because we can easily parallelize the SMC step, inferring the marginals $P[X_i(t)|F_i; \tilde{\theta}_i]$ and estimating the parameters θ_i for each neuron on a separate processor. We will discuss the empirical accuracy of this approximation in the Results section.

2.5. Estimating the connectivity matrix. Computing the M-step for the connectivity matrix, \mathbf{w} , is an optimization problem with on the order of N^2 variables. The auxiliary function ~~Equation Eq.~~ (7) is concave in \mathbf{w} , and decomposes into N separable terms that may be optimized independently using standard ascent methods. To improve our estimates, we will incorporate two sources of strong *a priori* information via our prior $P(\mathbf{w})$: first, previous anatomical studies have established that connectivity in many neuroanatomical substrates is “sparse,” ~~that is i.e.~~, most neurons form synapses with only a fraction of their neighbors (Buhl et al., 1994; Thompson et al., 1988; Reyes et al., 1998; Feldmeyer et al., 1999; Gupta et al., 2000; Feldmeyer and Sakmann, 2000; Petersen and Sakmann, 2000; Binzegger et al., 2004; Song et al., 2005; Mishchenko et al., 2009), implying that many elements of the connectivity matrix \mathbf{w} are zero; see also (Paninski, 2004; Rigat et al., 2006; Pillow et al., 2008; Stevenson et al., 2008) for further discussion. Second, “Dale’s law” states that each of a neuron’s postsynaptic connections in ~~the~~ adult cortex (and many other brain areas) must all be of the same sign (either excitatory or inhibitory). Both of these priors are easy to incorporate in the M-step optimization, as we discuss below.

2.5.1. Imposing a sparse prior on the connectivity. It is ~~well known~~ ~~well-known~~ that imposing sparseness via an $L1$ -regularizer can dramatically reduce the amount of data necessary to accurately reconstruct sparse high-dimensional parameters (Tibshirani, 1996; Tipping, 2001; Donoho and Elad, 2003; Ng, 2004; Candes and Wakin, 2008; Mishchenko, 2009). We incorporate a prior of the form $\ln p(\mathbf{w}) = \text{const.} - \lambda \sum_{i,j} |w_{ij}|$, and additionally enforce the constraints $|w_{ij}| < L$, for a suitable constant L (since both excitatory and inhibitory cortical connections are known to be bounded in size). Since the penalty $\ln p(\mathbf{w})$ is concave, and the constraints $|w_{ij}| < L$ are convex, we may solve the resulting optimization problem in the M-step using standard convex optimization methods (Boyd and Vandenberghe, 2004). In addition, the problem retains its separable structure: the full optimization may be broken up into N smaller problems that may be solved independently.

2.5.2. Imposing Dale’s law on the connectivity. Enforcing Dale’s law requires us to solve a ~~nonconvex, nonseparable~~ ~~non-convex, non-separable~~ problem: we need to optimize the concave function $Q(\theta, \theta^{(l)}) + \ln P(\theta)$ under the ~~nonconvex, nonseparable~~ ~~non-convex, non-separable~~ constraint that all of the elements in any column of the matrix \mathbf{w} are of the same sign (either nonpositive or ~~non-negative~~ ~~nonnegative~~). It is difficult to solve this nonconvex problem exactly, but we have found that simple greedy methods are quite efficient in finding good approximate solutions.

Algorithm 1 Pseudocode for estimating connectivity from calcium imaging data using EM; η_1 and η_2 are user-defined convergence tolerance parameters.

```

while  $|\mathbf{w}^{(l)} - \mathbf{w}^{(l-1)}| > \eta_1$  do
  for all  $i = 1 \dots N$  do
    while  $|\hat{\theta}_i^{(l)} - \hat{\theta}_i^{(l-1)}| > \eta_2$  do
      Approximate  $P[X_i(t)|F_i; \tilde{\theta}_i]$  using SMC (Section 2.3)
      Perform the M-step for the intrinsic parameters  $\tilde{\theta}_i$  (Section 2.3)
    end while
  end for
  for all  $i = 1 \dots N$  do
    Approximate  $P[n_i(t), \mathbf{h}_i(t)|\mathbf{F}; \theta_i]$  using either the blockwise Gibbs
    method or the factorized approximation (Section 2.4)
  end for
  for all  $i = 1 \dots N$  do
    Perform the M-step for  $\{b_i, \mathbf{w}_i\}_{i \leq N}$  using separable convex optimization methods (Section 2.5)
  end for
end while

```

We begin with our original sparse solution, obtained as discussed in the previous subsection without enforcing Dale’s law. Then we assign each neuron as either excitatory or inhibitory, based on the weights we have inferred in the previous step: that is, neurons i whose inferred postsynaptic connections w_{ij} are largely positive are tentatively labeled excitatory, and neurons with largely inhibitory inferred postsynaptic connections are labeled inhibitory. Neurons which are highly ambiguous may be unassigned in the early iterations, to avoid making mistakes from which it might be difficult to recover. Given the assignments a_i ($a_i = 1$ for putative excitatory cells, -1 for inhibitory, and 0 for neurons which have not yet been assigned), we solve the convex, separable problem

$$(19) \quad \underset{a_i w_{ij} \geq 0, |w_{ij}| < L \ \forall i, j}{\operatorname{argmax}} \quad Q(\theta, \theta^{(l)}) - \lambda \sum_{ij} |w_{ij}|,$$

which may be handled using the standard convex methods discussed above. Given the new estimated connectivities \mathbf{w} , we can re-assign the labels a_i , or flip some randomly to check for local optima. We have found this simple approach to be effective in practice.

2.6. Specific implementation notes. Pseudocode summarizing our approach is given in Algorithm 1. As discussed in Section 2.3, the intrinsic parameters $\tilde{\theta}_i$ may be initialized effectively using the methods described in (Vogelstein et al., 2009); then the full parameter θ is estimated via EM, where we use the embedded-chain-within-blockwise-Gibbs approach discussed in Section 2.4 (or the cheaper factorized approximation described in Section 2.4.1) to obtain the sufficient statistics in the E step and the separable convex optimization methods discussed in Section 2.5 for the M step.

As emphasized above, the parallel nature of these EM steps is essential for making these computations tractable. We performed the bulk of our analysis on a 256-processor cluster of Intel Xeon L5430 based computers (2.66 GHz). For 10 minutes of simulated fluorescence data, imaged at 30 Hz, calculations using the factorized approximation typically took 10-20 minutes per neuron (divided by the number of available processing nodes on the cluster), with time split approximately equally between (i) estimating the intrinsic parameters $\tilde{\theta}_i$, (ii) approximating the posteriors using the independent SMC method, and (iii) estimating the connectivity matrix, \mathbf{w} . The hybrid embedded-chain-within-blockwise-Gibbs sampler was substantially

slower, up to an hour per neuron, with the Gibbs sampler dominating the computation time, because we thinned the chain by a factor of five, following preliminary quantification of the autocorrelation timescale of the Gibbs chain (data not shown).

2.7. Simulating a neural population. To test the described method for inferring connectivity from calcium imaging data, we simulated networks of spontaneously firing randomly connected neurons according to our model, [Equations](#)~~Eqs.~~ (1-5), and also using other network models (see section 3.4). Although simulations ran at 1 msec time discretization, the imaging rate was assumed to be much slower: 5–200 Hz (~~cf. e.g. Fig.~~ [Figure](#) 8 below).

Model parameters were chosen based on experimental data available in the literature for cortical neural networks (Sayer et al., 1990; Braitenberg and Schuz, 1998; Gomez-Urquijo et al., 2000; Lefort et al., 2009). More specifically, the network consisted of 80% excitatory and 20% inhibitory neurons (Braitenberg and Schuz, 1998; Gomez-Urquijo et al., 2000), each respecting Dale’s law (as discussed in section 2.5 above). Neurons were randomly connected to each other in a spatially homogeneous manner with probability 0.1 (Braitenberg and Schuz, 1998; Lefort et al., 2009). Synaptic weights for excitatory connections, as defined by excitatory postsynaptic potential (PSP) peak amplitude, were randomly drawn from an exponential distribution with the mean of 0.5 mV (Lefort et al., 2009; Sayer et al., 1990). Inhibitory connections were also drawn from an exponential distribution, ~~÷~~ their strengths chosen so as to balance excitatory and inhibitory currents in the network, and achieve an average firing rate of ≈ 5 Hz (Abeles, 1991). Practically, this meant that the mean strength of inhibitory connections was about 10 times larger than that of the excitatory connections. PSP shapes were modeled as an alpha function (Koch, 1999): roughly, the difference of two exponentials, corresponding to a sharp rise and relatively slow decay (Sayer et al., 1990). We neglected conduction delays, given that the time delays below ~ 1 msec expected in the local cortical circuit were far below the time resolution of our simulated imaging data.

Note that PSP peak amplitudes measured *in vitro* [~~(as in, e.g., (Song et al., 2005))~~] ~~cannot~~ be incorporated directly in [Equation](#)~~Eq.~~ (1), since the synaptic weights in our model — w_{ij} in [Equation](#)~~Eq.~~ (1) — are dimensionless quantities representing the change in the spiking probability of neuron i given a spike in neuron j , whereas PSP peak amplitude describes the physiologically measured change in the membrane voltage of a neuron due to synaptic currents triggered by a spike in neuron j . To relate the two, note that in order to trigger an immediate spike in a neuron that typically has its membrane voltage V_b mV below the spiking threshold, roughly $n_E = V_b/V_E$ simultaneous excitatory PSPs with the peak amplitude V_E would be necessary. Therefore, the change in the spiking probability of a neuron due to excitatory synaptic current V_E can be approximately defined as

$$(20) \quad \delta P_E = V_E/V_b$$

(so that $\delta P_E n_E \approx 1$). $V_b \approx 15$ mV here, while values for the PSP amplitude V_E were chosen as described above. Similarly, according to [Equation](#)~~Eq.~~ 1, the same change in the spiking probability of a neuron i following the spike of a neuron j in the GLM is roughly

$$(21) \quad \delta P_E = [f(b_i + w_{ij}) - f(b_i)] \tau_h,$$

where recall τ_h is the typical PSP time-scale, ~~that is, i.e.~~ [the time over which a spike in neuron \$j\$ significantly affects the firing probability of the neuron \$i\$](#) . Equating these two expressions gives us a simple method for converting the physiological parameters V_E and V_b into suitable GLM parameters w_{ij} .

Finally, parameters for the internal calcium dynamics and fluorescence observations were chosen according to our experience with several cells analyzed using the algorithm of (Vogelstein et al., 2009), and conformed to previously published results (Yuste et al., 2006; Helmchen et al., 1996; Brenowitz and Regehr, 2007). Table 1 summarizes the details for each of the parameters in our model.

TABLE 1

Table of simulation parameters. $\mathcal{E}(\lambda)$ indicates an exponential distribution with mean λ , and $\mathcal{N}_p(\mu, \sigma^2)$ indicates a normal distribution with mean μ and variance σ^2 , truncated at lower bound $p\mu$. Units (when applicable) are given with respect to mean values (i.e., units are squared for variance).

| Variable | Value/Distribution | Unit |
|--------------------------------------|---------------------------------------|---------------|
| Total neurons | 10-500 | # |
| Excitatory neurons | 80 | % |
| Connections sparseness | 10 | % |
| Baseline firing rate | 5 | Hz |
| Excitatory PSP peak height | $\sim \mathcal{E}(0.5)$ | mV |
| Inhibitory PSP peak height | $\sim -\mathcal{E}(2.3)$ | mV |
| Excitatory PSP rise time | 1 | msec |
| Inhibitory PSP rise time | 1 | msec |
| Excitatory PSP decay time | $\sim \mathcal{N}_{0.5}(10, 2.5)$ | msec |
| Inhibitory PSP decay time | $\sim \mathcal{N}_{0.5}(20, 5)$ | msec |
| Refractory time, w_{ii} | $\sim \mathcal{N}_{0.5}(10, 2.5)$ | msec |
| Calcium std. σ_c | $\sim \mathcal{N}_{0.4}(28, 10)$ | μM |
| Calcium jump after spike, A_c | $\sim \mathcal{N}_{0.4}(80, 20)$ | μM |
| Calcium baseline, C_b | $\sim \mathcal{N}_{0.4}(24, 8)$ | μM |
| Calcium decay time, τ_c | $\sim \mathcal{N}_{0.4}(200, 60)$ | msec |
| Dissociation constant, K_d | 200 | μM |
| Fluorescence scale, α | 1 | n/a |
| Fluorescence baseline, β | 0 | n/a |
| Signal-dependent noise, γ | 10^{-3} - 10^{-5} | n/a |
| Signal-independent noise, σ^F | $4 \cdot 10^{-3}$ - $4 \cdot 10^{-5}$ | n/a |

3. Results. In this section we study the performance of our proposed network estimation methods, using the simulated data described in section 2.7 above. Specifically, we estimated the connectivity matrix using both the embedded-chain-within-blockwise-Gibbs approach and the simpler factorized approximation. Figure 4 summarizes one typical experiment: the EM algorithm using the factorized approximation estimated the connectivity matrix about as accurately as the full embedded-chain-within-blockwise-Gibbs approach ($r^2 = 0.47$ versus $r^2 = 0.48$). Thus, in the following we will focus primarily ~~primarily~~ on the factorized approximation, since this is much faster than the full blockwise-Gibbs approach (recall section 2.6).

3.1. Impact of coarse time discretization of calcium imaging data and scale factor of inferred connection weights. A notable feature of the results illustrated in the left panel of ~~Figure~~ Fig. 4 is that our estimator is biased downward ~~downwards~~ by a roughly constant scale factor: our estimates \hat{w}_{ij} are approximately linearly related to the true values of w_{ij} in the simulated network, but the slope of this linear relationship is less than one. At first blush, this bias does not seem like a major problem: as we discussed in section 2.7, even in the noiseless case we should at best expect our estimated coupling weights \hat{w}_{ij} to correspond to some monotonically increasing function of the true neural connectivities, as measured by biophysical quantities such as the peak PSP amplitude. Nonetheless, we would like to understand the

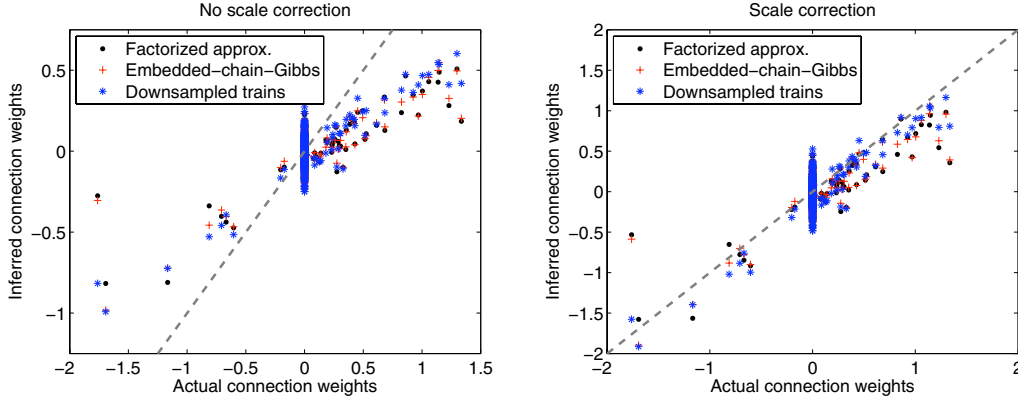


FIG 4. Quality of the connectivity matrix estimated from simulated calcium imaging data. Inferred connection weights \hat{w}_{ij} are shown in a scatter plot versus real connection weights w_{ij} , with inference performed using the factorized approximation, exact embedded-chain-within-blockwise-Gibbs approach, and true spike trains down-sampled to the frame rate of the calcium imaging. A network of $N = 25$ neurons was used, firing at ≈ 5 Hz, and imaged for $T = 10$ min at 60 Hz with intermediate $e\text{SNR} \approx 6$ (see Equation Eq. (6) and Figure 9 below). The squared correlation coefficient between the connection weights calculated using the factorized approximation and true connection weights was $r^2 = 0.47$, compared with the embedded-chain-within-blockwise-Gibbs method's $r^2 = 0.48$. For connection weights calculated directly from the true spike train down-sampled to the calcium imaging frame rate, we obtained $r^2 = 0.57$. (For comparison, $r^2 = 0.71$ for the connectivity matrix calculated using the full spike trains with 1 ms precision; data not shown.) Here and in the following figures the gray dashed line indicates unity, $y = x$. The inferred connectivity in the left panel shows a clear scale bias, which can be corrected by dividing by the scale correction factor calculated in section 3.1 below (right panel). The vertical lines apparent at zero in both subplots are due to the fact that the connection probability in the true network was significantly less than one: ~~that is~~, many of the true weights w_{ij} are exactly zero.

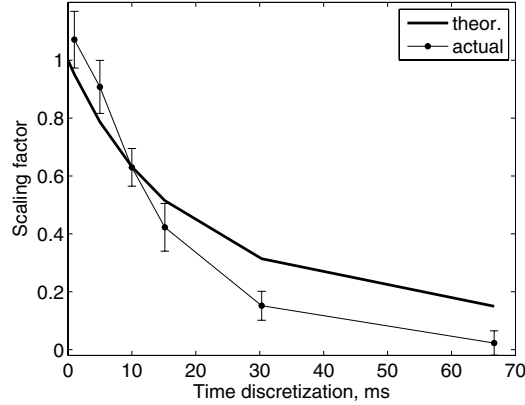


FIG 5. The low frame rate of calcium imaging explains the scale error observed in the inferred connectivity weights shown in Figure 4. A correction scale factor may be calculated analytically (thick line) as discussed in the main text (Equation Eq. 25). The scale error observed empirically (thin line) matches well with this theoretical estimate. In the latter case, the scale error was calculated from the fits obtained directly from the true spike trains, down sampled to different Δ , for a network of $N = 25$ neurons firing at ≈ 5 Hz and observed for $T = 10$ min. The error-bars indicate 95% confidence intervals for scale error at each Δ .

source of this bias more quantitatively; in this section ~~we~~ we discuss this issue in more depth and derive a simple method for correcting the bias.

The bias is largely due to the fact that we suffer a loss of temporal resolution when we

attempt to infer spike times from slowly-sampled fluorescence data. As discussed in (Vogelstein et al., 2009), we can recover some of this temporal information by using a finer time resolution for our recovered spike trains than Δ , the time resolution of the observed fluorescence signal. However, when we attempted to infer \mathbf{w} directly spike trains sampled from the posterior $P[\mathbf{X}|\mathbf{F}]$ at higher-than- Δ resolution, we found that the inferred connectivity matrix was strongly biased ~~toward~~ ~~towards~~ the symmetrized matrix $(\mathbf{w} + \mathbf{w}^T)/2$ (data not shown). In other words, whenever a nearly synchronous jump was consistently observed in two fluorescent traces $F_i(t)$ and $F_j(t)$ (at the reduced time resolution Δ), the EM algorithm would typically infer an excitatory *bidirectional* connection: ~~that is, i.e.~~, both \hat{w}_{ij} and \hat{w}_{ji} would be large, even if only a unidirectional connection existed between neurons i and j in the true network. While we expect, by standard arguments, that the Monte Carlo EM estimator constructed here should be consistent (i.e., we should recover the correct \mathbf{w} in the limit of large data length T and many Monte Carlo samples), we found that this bias persisted given experimentally-reasonable lengths of data and computation time.

Therefore, to circumvent this problem, we simply used the original imaging time resolution Δ for the inferred spike trains: note that, due to the definition of the spike history terms h_{ij} in ~~Equation Eq.~~ (3), a spike in neuron j at time t will only affect neuron i 's firing rate at time $t + \Delta$ and greater. This successfully counteracted the symmetrization problem (and also sped the calculations substantially), but resulted in the scale bias exhibited in Figure 4, since any spikes that fall into the same time bin are treated as coincidental: only spikes that precede spikes in a neighboring neuron by at least one time step will directly affect the estimates of w_{ij} , and therefore grouping asynchronous spikes within a single time bin Δ results in a loss of information.

To estimate the magnitude of this time-discretization bias more quantitatively, we consider a significantly simplified case of two neurons coupled with a small weight w_{12} , and firing with baseline firing rate of $r = f(b)$. In this case an approximate sufficient statistic for estimating w_{12} may be defined as the expected elevation in the spike rate of neuron one on an interval of length \mathcal{T} , following a spike in neuron two:

$$(22) \quad \begin{aligned} SS &= E \left[\int_{t'}^{t'+\mathcal{T}} n_1(t) dt \mid n_2(t') = 1, n_2(t) = 0 \ \forall t \in (t', t' + \mathcal{T}) \right] \\ &\approx r\mathcal{T} + f'(b)w_{12}\tau_h, \end{aligned}$$

where $f'(b)$ represents the slope of the nonlinear function $f(\cdot)$ at the baseline level b . This approximation leads to a conceptually simple method-of-moments estimator,

$$(23) \quad \hat{w}_{12} = (SS - r\mathcal{T})/f'(b)\tau_h.$$

Now, if the spike trains are down-sampled into time-bins of size Δ , we must estimate the statistic SS with a discrete sum instead:

$$(24) \quad \begin{aligned} SS^{ds} &= E \left[\sum_{t=t'+\Delta}^{t'+\Delta+\mathcal{T}} n_1^{ds}(t) \mid n_2^{ds}(t') = 1, n_2^{ds}(t) = 0 \ \forall t \in (t', t' + \mathcal{T}) \right] \\ &\approx r\mathcal{T} + f'(b) \int_0^{\Delta} \frac{dt'}{\Delta} \int_{t'}^{t'+\mathcal{T}} w_{12} \exp(-(t - t')/\tau_h) dt \\ &\approx r\mathcal{T} + f'(b)w_{12} \frac{1 - \exp(-\Delta/\tau_h)}{\Delta/\tau_h^2}. \end{aligned}$$

$n^{ds}(t)$ here are down-sampled spikes, ~~that is, i.e.~~ the spikes defined on a grid $t = 0, \Delta, 2\Delta, \dots$. In the second equality we made the approximation that the true position of the spike of

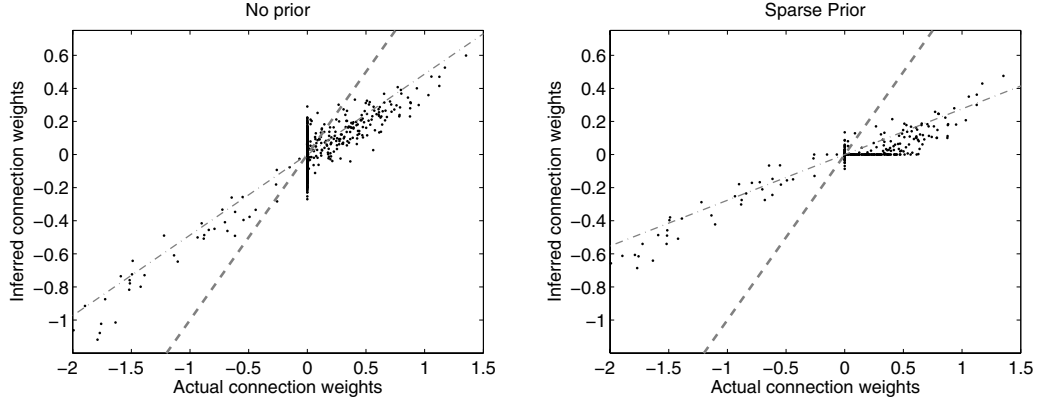


FIG 6. *Imposing a sparse prior on connectivity improves our estimates. Scatter plots indicate the connection weights w_{ij} reconstructed using no prior ($r^2 = 0.64$; left panel) and a sparse prior ($r^2 = 0.85$; right panel) vs. the true connection weights in each case. These plots were based on a simulation of $N = 50$ neurons firing at ≈ 5 Hz, imaged for $T = 10$ min at 60 Hz, with $\text{eSNR} \approx 10$. Clearly, the sparse prior reduces the relative error, as indicated by comparing the relative distance between the data points (black dots) to the best linear fit (gray dash-dotted line), at the expense of some additional soft-threshold bias, as is usual in the L_1 setting.*

the second neuron, $n_2^{ds}(t')$, may be uniformly distributed in the first time-bin $[0, \Delta]$, and the discrete sum over t is from the second time-bin $[\Delta, 2\Delta]$ to $[\mathcal{T}, \mathcal{T} + \Delta]$, that is, i.e. over all spikes of the first neuron that occurred in any of the strictly subsequent time-bins up to $\mathcal{T} + \Delta$. Forming a method-of-moments estimator as in [EquationEq. 23](#) leads to a biased estimate, ÷

$$(25) \quad \hat{w}_{12}^{ds} \approx \frac{1 - \exp(-\Delta/\tau_h)}{\Delta/\tau_h} \hat{w}_{12},$$

and somewhat surprisingly (given the rather crude nature of these approximations), this corresponds quite well with the scale bias we observe in practice. In Figure 5 we plot the scale bias from [EquationEq. 25](#) versus that empirically deduced from our simulations for different values of Δ ; we see that [EquationEq. 25](#) describes the observed scale bias fairly well. Thus, we can divide by this analytically-derived factor to effectively correct the bias of our estimates, as shown in the right panel of [FigureFig. 4](#).

3.2. Impact of prior information on the inference. Next we investigated the importance of incorporating prior information in our estimates. We found that imposing a sparse prior (as described in section 2.5) significantly improved our results. For example, [FigureFig. 6](#) illustrates a case in which our obtained r^2 increased from 0.64 (with no L_1 penalization in the M-step) to 0.85 (with penalization; the penalty λ was chosen approximately as the inverse mean absolute value of w_{ij} , which is known here because we prepared the network simulations, but is available in practice given the previous physiological measurements discussed in section 2.7). See also [FigureFig. 10](#) below. Furthermore, the weights estimated using the sparse prior more reliably provide the sign (i.e., excitatory or inhibitory) of each presynaptic neuron in the network (Figure 7).

Incorporation of Dale's law, on the other hand, only leads to an $\approx 10\%$ change in the estimation r^2 in the absence of an L_1 penalty, and no significant improvement at all in the presence of an L_1 penalty (data not shown). Thus, Dale's prior was not pursued further here.

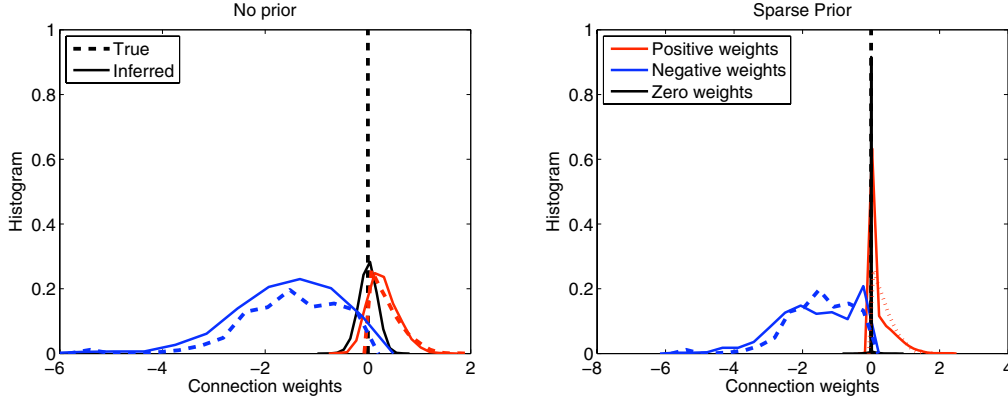


FIG 7. The distributions of inferred connection weights using no prior (left panel) and a sparse prior (right panel) vs. true distributions. When the sparse prior is enforced, zero weights are recovered with substantially higher frequency (black lines), thus allowing better identification of connected neural pairs. Likewise, excitatory and inhibitory weights are better recognized (red and blue lines, respectively), thus allowing accurate classification of neurons as excitatory or inhibitory. The normalized Hamming distance between the inferred and true connectivity matrix here $H(\mathbf{w}, \hat{\mathbf{w}}) = [N(N-1)]^{-1} \sum_{i,j} |\text{sign}(w_{ij}) - \text{sign}(\hat{w}_{ij})|$, with the convention $\text{sign}(0) = 0$ was 0.06. Distributions are shown for a simulated population of $N = 200$ neurons firing at ≈ 5 Hz and imaged for $T = 10$ min at 60 Hz, with $\text{eSNR} \approx 10$. Note that the peak at zero in the true distributions (black dashed trace) corresponds to the vertical line visible at zero in [Figures 4 and 6](#).

3.3. Impact of experimental factors on estimator accuracy. Next we sought to quantify the minimal experimental conditions necessary for accurate estimation of the connectivity matrix. Figure 8 shows the quality of the inferred connectivity matrix as a function of the imaging frame rate, and indicates that imaging frame rates ≥ 30 Hz are needed to achieve meaningful reconstruction results. This matches nicely with currently-available technology; as discussed in the introduction, 30 or 60 Hz imaging is already in progress in a number of laboratories (Nguyen et al., 2001; Iyer et al., 2006; Salome et al., 2006; Reddy et al., 2008), though in some cases higher imaging rates come at a cost in the signal-to-noise ratio of the images or in the number of neurons that may be imaged simultaneously. Similarly, Figure 9 illustrates the quality of the inferred connectivity matrix as a function of the effective SNR measure defined in [Equation 6](#).

Finally, Figure 10 shows the quality of the inferred connectivity matrix as a function of the experimental duration. The minimal amount of data for a particular r^2 depended substantially on whether the sparse prior was enforced. In particular, when not imposing a sparse prior, the calcium imaging duration necessary to achieve $r^2 = 0.5$ for the reconstructed connectivity matrix in this setting was $T \approx 10$ min, and $r^2 = 0.75$ was achieved at $T \approx 30$ min. With a sparse prior, $r^2 > 0.7$ was achieved already at $T \approx 5$ min. Furthermore, we observed that the accuracy of the reconstruction did not deteriorate dramatically with the size of the imaged neural population: roughly the same reconstruction quality was observed (given a fixed length of data) for N varying between 50–200 neurons. These results were consistent with a rough Fisher information computation which we performed but have omitted here to conserve space.

3.4. Impact of strong correlations and deviations from generative model on the inference. Estimation of network connectivity is fundamentally rooted in observing changes in the spike rate conditioned on the state of the other neurons. Considered from the point of view of estimating a standard GLM, it is clear that the inputs to our model (1) must satisfy certain basic

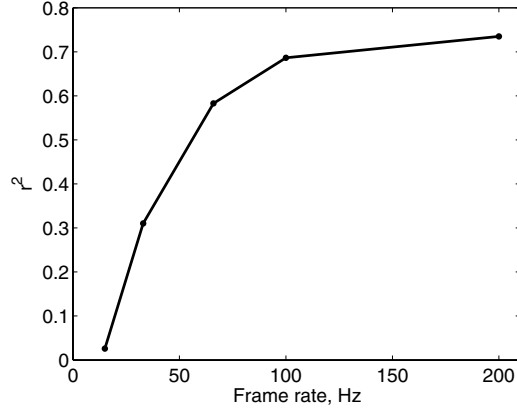


FIG 8. Accuracy of the inferred connectivity as a function of the frame rate of calcium imaging. A population of $N = 25$ neurons firing at ≈ 5 Hz and imaged for $T = 10$ min was simulated here, with $eSNR \approx 10$. At 100 Hz, r^2 saturated at the level $r^2 \approx 0.7$ achieved with $\Delta \rightarrow 0$.

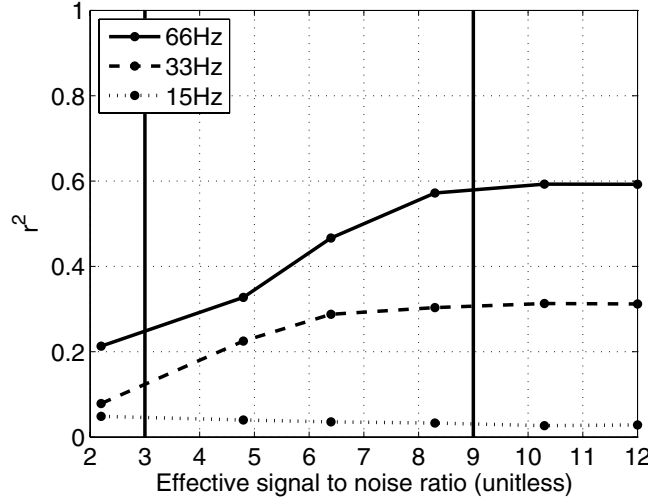


FIG 9. Accuracy of inferred connectivity as a function of effective imaging SNR ($eSNR$, defined in Equation 6), for frame rates of 15, 33, and 66 Hz. Neural population simulation was the same as in Figure 8. Vertical black lines correspond to the $eSNR$ values of the two example traces in Figure 3, for comparison.

identifiability conditions if we are to have any hope of accurately estimating the parameter \mathbf{w} . In particular, we must rule out highly multicollinear inputs $\{h_{ij}(t)\}$: speaking roughly, the set of observed spike trains should be rich enough to span all N dimensions of \mathbf{w}_i , for each cell i . In the simulations pursued here, the coupling matrix $\{w_{ij}\}_{i \neq j}$ was fairly weak and neurons fired largely independently of each other: see Figure 11, upper left, for an illustration. In this case of weakly-correlated firing, the inputs $\{h_{ij}(t)\}$ will also be weakly correlated, and the model should be identifiable, as indeed we found. Should this weak-coupling condition be violated, however (e.g., due to high correlations in the spiking of a few neurons), we may require much more data to obtain accurate estimates due to multicollinearity problems.

To explore this issue, we carried out a simulation of a hypothetical strongly coupled neural network, where, in addition to the physiologically-relevant weak sparse connectivity discussed

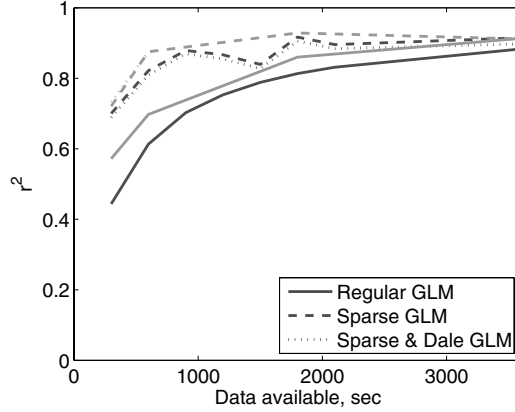


FIG 10. Accuracy of inferred connectivity as a function of the imaging time and neural population size. Incorporating a sparse prior dramatically increases the reconstruction quality (dashed lines). When the sparse prior is imposed, $T = 5$ min is sufficient to recover 70% of the variance in the connection weights. Incorporating Dale’s prior leads to only marginal improvement (dotted line). Furthermore, reconstruction accuracy does not strongly depend on the neural population size, N . Here, neural populations of size $N = 100$ and 200 are shown (black and gray, respectively), with $eSNR \approx 10$ and 60 Hz imaging rate in each case.

in section 2.7, we introduced a sparse random strong connectivity component. More specifically, we allowed a fraction of neurons to couple strongly to the other neurons, making these “command” neurons which in turn could strongly drive the activity of the rest of the population (MacLean et al., 2005). The strength of this strong connectivity component was chosen to dynamically build up the actual firing rate from the baseline rate of $f(b) \approx 1$ Hz to approximately 5 Hz. Such a network showed patterns of activity very different from the weakly coupled networks inspected above (Figure 11, top right). In particular, a large number of highly correlated events across many neurons were evident in this network. As expected, our algorithm was not able to identify the true connectivity matrix correctly in this scenario (Figure 11, bottom right panel). For ease of comparison, the left panels show a “typical” network (i.e., one lacking many strongly coupled neurons), and its associated connectivity inference.

On the other hand, our inference algorithm showed significant robustness to model misspecification, [that is i.e.](#), deviations from our generative model. One important such deviation is variation in the time scales of PSPs in different synapses. Up to now, all PSP time-scales were assumed to be the same, [that is i.e.](#), $\{\tau_{ij}^h\}_{i,j \leq N} = \tau_h$. In Figure 12 we introduce additional variability in τ_h from one neuron to another. Variability in τ_h results in added variance in the estimates of the connectivity weights, w_{ij} , through the τ_h -dependence of the scaling factor [Equation Eq.](#) (25). However, we found that this additional variance was relatively insignificant in cases where τ_h varied up to 25% from neuron to neuron. We also found that inference was robust to changes in the sparseness of the underlying connectivity matrix: we simulated neural populations of size $N = 25$ and $N = 50$ neurons, as above, with connection sparseness varying from 5% (very sparse) to 100% (all-to-all), and in all cases the performance of our algorithm remained stable, with $r^2 \approx 0.9$ for the estimate of the connected weights, $w_{ij} \neq 0$ (data not shown). Finally, simulations with more biophysically-based conductance-driven noisy integrate-and-fire network models (Vogels and Abbott, 2005) led to qualitatively similar results, further establishing the robustness of these methods; again, details are omitted to conserve space.

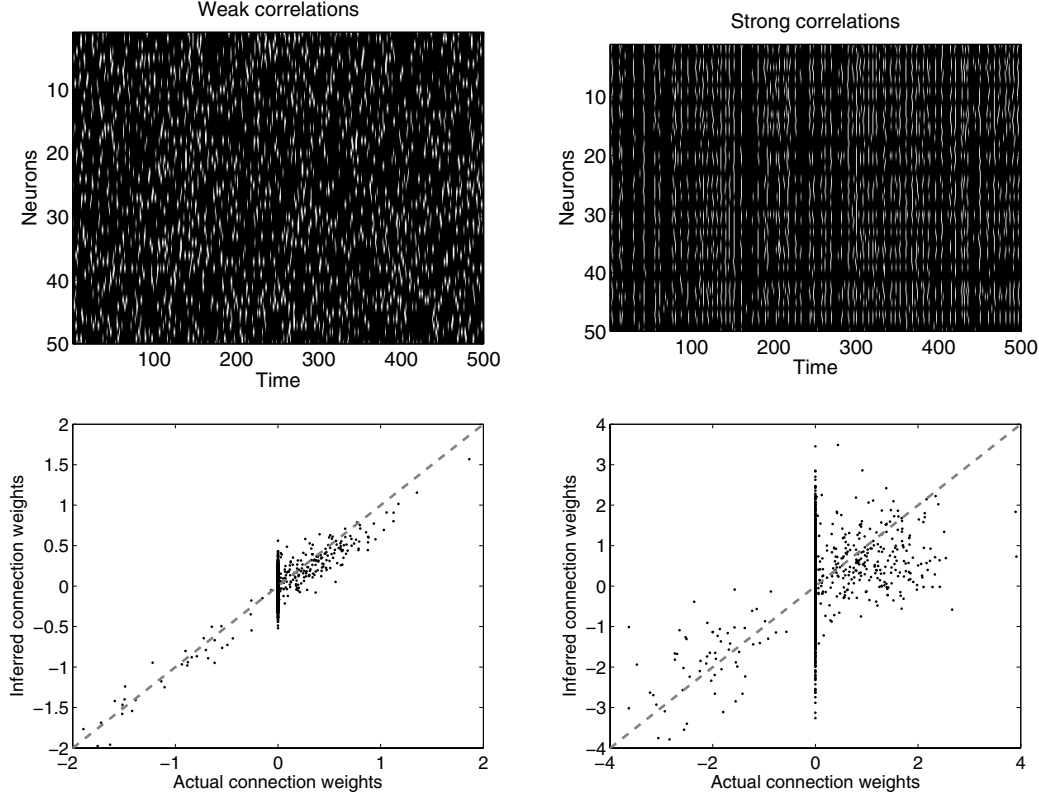


FIG 11. *Diversity of observed neural activity patterns is required for accurate circuit inference. Here, 15 sec of simulated spike trains for a weakly coupled network (top left panel) and a network with strongly coupled component (top right panel) are shown. In weakly coupled networks, spikes are sufficiently uncorrelated to give access to enough different neural activity patterns to estimate the weights \mathbf{w} . In a strongly coupled case, many highly synchronous events are evident (top right panel), thus preventing observation of a sufficiently rich ensemble of activity patterns. Accordingly, the connectivity estimates for the strongly coupled neural network (bottom right panel) ~~do not~~ represent the true connectivity of the circuit, even for the weakly coupled component. This is contrary to the weakly-coupled network (bottom left panel) where true connectivity is successfully obtained. Networks of $N = 50$ neurons firing at ≈ 5 Hz and imaged for $T = 10$ min at 60 Hz were used to produce this figure; $e\text{SNR} \approx 10$.*

4. Discussion. In this paper we develop a Bayesian approach for inferring connectivity in a network of spiking neurons observed using calcium fluorescent imaging. A number of previous authors have addressed the problem of inferring neuronal connectivity given a fully-observed set of spike trains in a network (Brillinger, 1988; Chornoboy et al., 1988; Brillinger, 1992; Paninski et al., 2004; Paninski, 2004; Truccolo et al., 2005; Rigat et al., 2006; Nykamp, 2007; Kulkarni and Paninski, 2007; Vidne et al., 2009; Stevenson et al., 2009; Garofalo et al., 2009; Cocco et al., 2009), but the main challenge in the present work is the indirect nature of the calcium imaging data, which provides only noisy, low-pass filtered, temporally sub-sampled observations of spikes of individual neurons. To solve this problem, we develop a specialized blockwise-Gibbs sampler that makes use of an embedded Markov chain method due to (Neal et al., 2003). The connectivity matrix is then inferred in an EM framework; the M-step parallelizes quite efficiently and allows for the easy incorporation of prior sparseness information, which significantly reduces data requirements in this context. We have found that these methods can effectively infer the connectivity in simulated neuronal networks, given

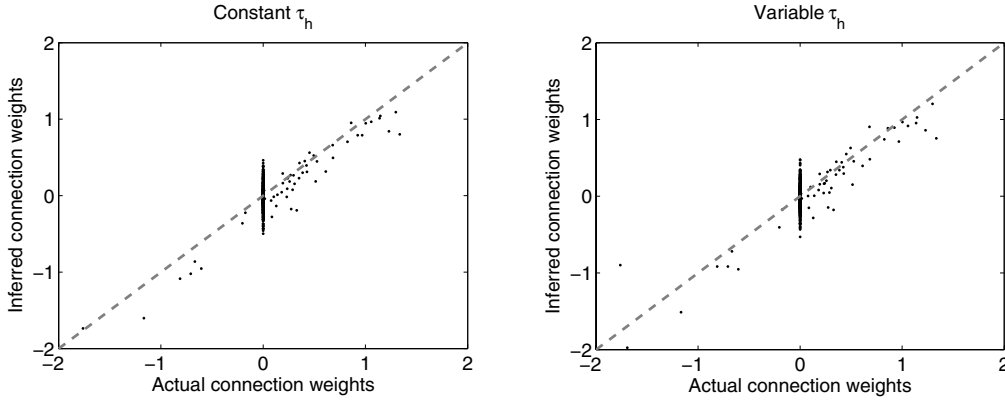


FIG 12. *Inference is robust to deviations of the data from our generative model. With up to 25% variability allowed in PSP time scales τ_h (right panel), our algorithm provided reconstructions of almost the same quality as when all τ_h 's were the same (left panel). Simulation conditions were the same as in Figure 8, at 60 Hz imaging rate.*

reasonable lengths of data, computation time, and assumptions on the biophysical network parameters.

To our knowledge, we are the first to address this problem using the statistical deconvolution methods and EM formulation described here [although see also (Roxin et al., 2008), who fit simplified, low temporal resolution transition-based models to the 10 Hz calcium data obtained by (Ikegaya et al., 2004)]. However, we should note that (Rigat et al., 2006) developed a closely related approach to infer connectivity from low-SNR electrical recordings involving possibly-misclassified spikes (in contrast to the slow, lowpass-filtered calcium signals we discuss here). In particular, these authors employed a very similar Bernoulli GLM and developed a Metropolis-within-Gibbs sampler to approximate the necessary sufficient statistics for their model. In addition, (Rigat et al., 2006) develop a more intricate hierarchical prior for the connectivity parameter \mathbf{w} ; while we found that a simple L_1 penalization was quite effective here, it will be worthwhile to explore more informative priors in future work.

A number of possible improvements of our method are available. One of the biggest challenges for inferring neural connectivity from functional data is the presence of indirect inputs from unobserved neurons (Nykamp, 2005; Nykamp, 2007; Kulkarni and Paninski, 2007; Vidne et al., 2009; Vakorin et al., 2009): it is typically impossible to observe the activity of all neurons in a given circuit, and correlations in the unobserved inputs can mimic connections among different observed neurons. Developing methods to cope with such unobserved common inputs is currently an area of active research, and should certainly be incorporated in the methods we have developed here.

Several other important directions for future work are worth noting. First, recently-developed photo-stimulation methods for activating or deactivating individual neurons or sub-populations (Boyden et al., 2005; Szobota et al., 2007; Nikolenko et al., 2008) may be useful to increase statistical power in cases where the circuit's unperturbed activity may not allow reliable determination of a circuit's connectivity matrix; in particular, by utilizing external stimulation, we can in principle choose a sufficiently rich experimental design (i.e., a sample of input activity patterns) to overcome the multicollinearity problems discussed in the context of Figure 11.

Second, improvements of the algorithms for faster implementation are under development. Specifically, fast non-negative optimization-based deconvolution methods may be a promis-

ing alternative (Vogelstein et al., 2008; Paninski et al., 2009) to the SMC approach used here. In addition, modifications of our generative model to incorporate [nonstationarities](#) ~~non-stationarities~~ in the fluorescent signal (e.g., due to dye bleaching and drift) are fairly straightforward.

Third, a fully Bayesian algorithm for estimating the posterior distributions of all the parameters (instead of just the MAP estimate) would be of significant interest. Such a fully-Bayesian extension is conceptually simple: we just need to extend our Gibbs sampler to additionally sample from the parameter θ given the sampled spike trains \mathbf{X} . Since we already have a method for drawing \mathbf{X} given θ and \mathbf{F} , with such an additional sampler we may obtain samples from $P(\mathbf{X}, \theta | \mathbf{F})$ simply by sampling from $\mathbf{X} \sim P(\mathbf{X} | \theta, \mathbf{F})$ and $\theta \sim P(\theta | \mathbf{X})$, via blockwise-Gibbs. Sampling from the posteriors $P(\theta | \mathbf{X})$ in the GLM setting is quite tractable using hybrid Monte Carlo methods, since all of the necessary posteriors are log-concave (Ishwaran, 1999; Gamerman, 1997; Gamerman, 1998; Ahmadian et al., 2009).

Finally, most importantly, we are currently applying these algorithms in preliminary experiments on real data. Checking the accuracy of our estimates is of course more challenging in the context of [nonsimulated](#) ~~non-simulated~~ data, but a number of methods for partial validation are available, including multiple-patch recordings (Song et al., 2005), [photo stimulation](#) ~~photostimulation~~ techniques (Nikolenko et al., 2007), and fluorescent anatomical markers which can distinguish between different cell types (Meyer et al., 2002) (i.e., inhibitory vs. excitatory cells; ~~cf. Figure 7~~ [Figure 7](#)). We hope to present our results in the near future.

[Acknowledgments](#)~~**Acknowledgements**~~. We thank R. Yuste, B. Watson, A. Packer, T. Sippy, T. Mrsic-Flogel, and V. Bonin for data and helpful discussions, and A. Ramirez for helpful comments on an earlier draft. LP is supported by an NSF CAREER and McKnight Scholar award; JV by NIDCD grant DC00109.

References.

- Abeles, M. (1991). *Corticonics*. Cambridge University Press.
- Ahmadian, Y., Pillow, J., and Paninski, L. (2009). Efficient Markov Chain Monte Carlo methods for decoding population spike trains. *Under review, Neural Computation*.
- Andrieu, C., Doucet, A., and Holenstein, A. (2007). Particle Markov chain Monte Carlo. *Working paper*.
- Bickel, P., Li, B., and Bengtsson, T. (2008). Sharp failure rates for the bootstrap particle filter in high dimensions. In Clarke, B. and Ghosal, S., editors, *Pushing the Limits of Contemporary Statistics: Contributions in Honor of Jayanta K. Ghosh*, pages 318–329. IMS.
- Binzegger, T., Douglas, R. J., and Martin, K. A. C. (2004). A Quantitative Map of the Circuit of Cat Primary Visual Cortex. *J. Neurosci.*, 24(39):8441–8453.
- Boyd, S. and Vandenberghe, L. (2004). *Convex Optimization*. Oxford University Press.
- Boyden, E. S., Zhang, F., Bamberg, E., Nagel, G., and Deisseroth, K. (2005). Millisecond-timescale, genetically targeted optical control of neural activity. *Nat Neurosci.*, 8(9):1263–1268.
- Braitenberg, V. and Schuz, A. (1998). *Cortex: statistics and geometry of neuronal connectivity*. Springer, Berlin.
- Brenowitz, S. D. and Regehr, W. G. (2007). Reliability and heterogeneity of calcium signaling at single presynaptic boutons of cerebellar granule cells. *J Neurosci.*, 27(30):7888–7898.

- Briggman, K. L. and Denk, W. (2006). Towards neural circuit reconstruction with volume electron microscopy techniques. *Current Opinions in Neurobiology*, 16:562.
- Brillinger, D. (1988). Maximum likelihood analysis of spike trains of interacting nerve cells. *Biological Cyberkinetics*, 59:189–200.
- Brillinger, D. (1992). Nerve cell spike train data analysis: a progression of technique. *Journal of the American Statistical Association*, 87:260–271.
- Buhl, E., Halasy, K., and Somogyi, P. (1994). Diverse sources of hippocampal unitary inhibitory postsynaptic potentials and the number of synaptic release sites. *Nature*, 368:823–828.
- Candes, E. J. and Wakin, M. (2008). An introduction to compressive sampling. *IEEE Signal Processing Magazine*, 25(2):21–30.
- Chornoboy, E., Schramm, L., and Karr, A. (1988). Maximum likelihood identification of neural point process systems. *Biological Cybernetics*, 59:265–275.
- Cocco, S., Leibler, S., and Monasson, R. (2009). Neuronal couplings between retinal ganglion cells inferred by efficient inverse statistical physics methods. *Proceedings of the National Academy of Sciences*, 106(33):14058–14062.
- Cossart, R., Aronov, D., and Yuste, R. (2003). Attractor dynamics of network up states in the neocortex. *Nature*, 423:283–288.
- Dempster, A., Laird, N., and Rubin, D. (1977). Maximum likelihood from incomplete data via the EM algorithm. *Journal Royal Stat. Soc., Series B*, 39:1–38.
- Djurisic, M., Antic, S., Chen, W. R., and Zecevic, D. (2004). Voltage imaging from dendrites of mitral cells: EPSP attenuation and spike trigger zones. *J. Neurosci.*, 24(30):6703–6714.
- Dombeck, D. A., Khabbazz, A. N., Collman, F., Adelman, T. L., and Tank, D. W. (2007). Imaging large-scale neural activity with cellular resolution in awake, mobile mice. *Neuron*, 56(1):43–57.
- Donoho, D. and Elad, M. (2003). Optimally sparse representation in general (nonorthogonal) dictionaries via L^1 minimization. *PNAS*, 100:2197–2202.
- Douc, R., Cappe, O., and Moulines, E. (2005). Comparison of resampling schemes for particle filtering. *Proc. 4th Int. Symp. Image and Signal Processing and Analysis*.
- Doucet, A., de Freitas, N., and Gordon, N., editors (2001). *Sequential Monte Carlo in Practice*. Springer.
- Doucet, A., Godsill, S., and Andrieu, C. (2000). On sequential Monte Carlo sampling methods for Bayesian filtering. *Statistics and Computing*, 10:197–208.
- Escola, S. and Paninski, L. (2008). Hidden Markov models applied toward the inference of neural states and the improved estimation of linear receptive fields. *Under review, Neural Computation*.
- Feldmeyer, D., Egger, V., Lubke, J., and Sakmann, B. (1999). Reliable synaptic connections between pairs of excitatory layer 4 neurones within a single “barrel” of developing rat somatosensory cortex. *J Physiol*, 521 Pt 1:169–90.
- Feldmeyer, D. and Sakmann, B. (2000). Synaptic efficacy and reliability of excitatory connections between the principal neurones of the input (layer 4) and output layer (layer 5) of the neocortex. *J Physiol*, 525:31–9.
- Gamerman, D. (1997). Sampling from the posterior distribution in generalized linear mixed models. *Statistics and Computing*, 7(1):57–68.
- Gamerman, D. (1998). Markov chain monte carlo for dynamic generalised linear models. *Biometrika*, 85(1):215–227.
- Garofalo, M., Nieuws, T., Massobrio, P., and Martinoia, S. (2009). Evaluation of the perfor-

- mance of information theory-based methods and cross-correlation to estimate the functional connectivity in cortical networks. *PLoS ONE*, 4:e6482.
- Godsill, S., Doucet, A., and West, M. (2004). Monte Carlo smoothing for non-linear time series. *Journal of the American Statistical Association*, 99:156–168.
- Gomez-Urquijo, S. M., Reblet, C., Bueno-Lopez, J. L., and Gutierrez-Ibarluzea, I. (2000). Gabaergic neurons in the rabbit visual cortex: percentage, distribution and cortical projections. *Brain Res*, 862:171–9.
- Greenberg, D. S., Houweling, A. R., and Kerr, J. N. D. (2008). Population imaging of ongoing neuronal activity in the visual cortex of awake rats. *Nat Neurosci*.
- Gupta, A., Wang, Y., and Markram, H. (2000). Organizing principles for a diversity of gabaergic interneurons and synapses in the neocortex. *Science*, 287:273–8.
- Harris, K., Csicsvari, J., Hirase, H., Dragoi, G., and Buzsaki, G. (2003). Organization of cell assemblies in the hippocampus. *Nature*, 424:552–556.
- Hatsopoulos, N., Ojakangas, C., Paninski, L., and Donoghue, J. (1998). Information about movement direction obtained by synchronous activity of motor cortical neurons. *PNAS*, 95:15706–15711.
- Helmchen, F., Imoto, K., and Sakmann, B. (1996). Ca^{2+} buffering and action potential-evoked Ca^{2+} signaling in dendrites of pyramidal neurons. *Biophys J*, 70(2):1069–1081.
- Ikegaya, Y., Aaron, G., Cossart, R., Aronov, D., Lampl, I., Ferster, D., and Yuste, R. (2004). Synfire chains and cortical songs: temporal modules of cortical activity. *Science*, 304(5670):559–564.
- Ishwaran, H. (1999). Applications of hybrid Monte Carlo to Bayesian generalized linear models: quasicomplete separation and neural networks. *Journal of Computational and Graphical Statistics*, 8:779–799.
- Iyer, V., Hoogland, T. M., and Saggau, P. (2006). Fast functional imaging of single neurons using random-access multiphoton (RAMP) microscopy. *J Neurophysiol*, 95(1):535–545.
- Koch, C. (1999). *Biophysics of Computation*. Oxford University Press.
- Kulkarni, J. and Paninski, L. (2007). Common-input models for multiple neural spike-train data. *Network: Computation in Neural Systems*, 18:375–407.
- Lefort, S., Tómm, C., Floyd Sarria, J.-C., and Petersen, C. C. H. (2009). The excitatory neuronal network of the c2 barrel column in mouse primary somatosensory cortex. *Neuron*, 61:301–16.
- Lei, N., Watson, B., MacLean, J., Yuste, R., and Shepard, K. (2008). A 256-by-256 cmos microelectrode array for extracellular stimulation of acute brain slices. *Proceedings to the International Solid-State Circuits Conference*.
- Li, K. and Duan, N. (1989). Regression analysis under link violation. *Annals of Statistics*, 17:1009–1052.
- Litke, A., Bezayiff, N., Chichilnisky, E., Cunningham, W., Dabrowski, W., Grillo, A., Grivich, M., Grybos, P., Hottowy, P., Kachiguine, S., Kalmar, R., Mathieson, K., Petrusca, D., Rahman, M., and Sher, A. (2004). What does the eye tell the brain? development of a system for the large scale recording of retinal output activity. *IEEE Trans Nucl Sci*, pages 1434–1440.
- Livet, J., Weissman, T., Kang, H., Draft, R., Lu, J., Bennis, R., Sanes, J., and Lichtman, J. (2007). Transgenic strategies for combinatorial expression of fluorescent proteins in the nervous system. *Nature*, 450:56–62.
- Luczak, A., Bartho, P., Marguet, S., Buzsaki, G., and Harris, K. (2007). Sequential structure of neocortical spontaneous activity in vivo. *PNAS*, 104:347–352.

- MacLean, J., Watson, B., Aaron, G., and Yuste, R. (2005). Internal dynamics determine the cortical response to thalamic stimulation. *Neuron*, 48:811–823.
- McLachlan, G. and Krishnan, T. (1996). *The EM Algorithm and Extensions*. Wiley-Interscience.
- Meyer, A. H., Katona, I., Blatow, M., Rozov, A., and Monyer, H. (2002). In Vivo Labeling of Parvalbumin-Positive Interneurons and Analysis of Electrical Coupling in Identified Neurons. *J. Neurosci.*, 22:7055–7064.
- Micheva, K. and Smith, S. (2007). Array tomography: A new tool for imaging the molecular architecture and ultrastructure of neural circuits. *Neuron*, 55:25–36.
- Mishchenko, Y. (2009). Strategies for identifying exact structure of neural circuits with broad light microscopy connectivity probes. *Preprint*: <http://precedings.nature.com/documents/2669/version/2>.
- Mishchenko, Y., Spacek, J., Mendenhall, J., Chklovskii, D., and Harris, K. M. (2009). Reconstruction of hippocampal CA1 neuropil at nanometer resolution reveals disordered packing of processes and dependence of synaptic connectivity on local environment and dendritic caliber. *Submitted*.
- Neal, R., Beal, M., and Roweis, S. (2003). Inferring state sequences for non-linear systems with embedded hidden Markov models. *NIPS*, 16.
- Ng, A. (2004). Feature selection, L_1 vs. L_2 regularization, and rotational invariance. *ICML*, 21.
- Nguyen, Q. T., Callamaras, N., Hsieh, C., and Parker, I. (2001). Construction of a two-photon microscope for video-rate Ca^{2+} imaging. *Cell Calcium*, 30(6):383–393.
- Nikolenko, V., Poskanzer, K., and Yuste, R. (2007). Two-photon photostimulation and imaging of neural circuits. *Nature Methods*, 4:943–950.
- Nikolenko, V., Watson, B., Araya, R., Woodruff, A., Peterka, D., and Yuste, R. (2008). SLM microscopy: Scanless two-photon imaging and photostimulation using spatial light modulators. *Frontiers in Neural Circuits*, In press.
- Nykamp, D. (2007). A mathematical framework for inferring connectivity in probabilistic neuronal networks. *Mathematical Biosciences*, 205:204–251.
- Nykamp, D. Q. (2005). Revealing pairwise coupling in linear-nonlinear networks. *SIAM J Applied Mathematics*, 65(6):2005–2032.
- Ohki, K., Chung, S., Ch’ng, Y., Kara, P., and Reid, C. (2005). Functional imaging with cellular resolution reveals precise micro-architecture in visual cortex. *Nature*, 433:597–603.
- Paninski, L. (2004). Maximum likelihood estimation of cascade point-process neural encoding models. *Network: Computation in Neural Systems*, 15:243–262.
- Paninski, L., Ahmadian, Y., Ferreira, D., Koyama, S., Rahnama, K., Vidne, M., Vogelstein, J., and Wu, W. (2009). A new look at state-space models for neural data. *Journal of Computational Neuroscience*, In press.
- Paninski, L., Fellows, M., Shoham, S., Hatsopoulos, N., and Donoghue, J. (2004). Superlinear population encoding of dynamic hand trajectory in primary motor cortex. *J. Neurosci.*, 24:8551–8561.
- Petersen, C. C. and Sakmann, B. (2000). The excitatory neuronal network of rat layer 4 barrel cortex. *J Neurosci*, 20(20):7579–86.
- Petrusca, D., Grivich, M. I., Sher, A., Field, G. D., Gauthier, J. L., Greschner, M., Shlens, J., Chichilnisky, E. J., and Litke, A. M. (2007). Identification and characterization of a Y-like primate retinal ganglion cell type. *J. Neurosci.*, 27(41):11019–11027.
- Pillow, J., Shlens, J., Paninski, L., Sher, A., Litke, A., Chichilnisky, E., and Simoncelli, E.

- (2008). Spatiotemporal correlations and visual signaling in a complete neuronal population. *Nature*, 454:995–999.
- Plesser, H. and Gerstner, W. (2000). Noise in integrate-and-fire neurons: From stochastic input to escape rates. *Neural Computation*, 12:367–384.
- Rabiner, L. (1989). A tutorial on hidden Markov models and selected applications in speech recognition. *Proceedings of the IEEE*, 77:257–286.
- Ramon y Cajal, S. (1904). *La Textura del Sistema Nerviosa del Hombre y los Vertebrados*. Moya.
- Ramon y Cajal, S. (1923). *Recuerdos de mi vida: Historia de mi labor cientifica*. Alianza Editorial.
- Reddy, G., Kelleher, K., Fink, R., and Saggau, P. (2008). Three-dimensional random access multiphoton microscopy for functional imaging of neuronal activity. *Nature Neuroscience*, 11(6):713–720.
- Reyes, A., Lujan, R., Rozov, A., Burnashev, N., Somogyi, P., and Sakmann, B. (1998). Target-cell-specific facilitation and depression in neocortical circuits. *Nat Neurosci*, 1:279–285.
- Rigat, F., de Gunst, M., and van Pelt, J. (2006). Bayesian modelling and analysis of spatio-temporal neuronal networks. *Bayesian Analysis*, 1:733–764.
- Robert, C. and Casella, G. (2005). *Monte Carlo Statistical Methods*. Springer.
- Roxin, A., Hakim, V., and Brunel, N. (2008). The statistics of repeating patterns of cortical activity can be reproduced by a model network of stochastic binary neurons. *J. Neurosci.*, 28(42):10734–10745.
- Salome, R., Kremer, Y., Dieudonne, S., Leger, J.-F., Krichevsky, O., Wyart, C., Chatenay, D., and Bourdieu, L. (2006). Ultrafast random-access scanning in two-photon microscopy using acousto-optic deflectors. *Journal of Neuroscience Methods*, 154(1-2):161–174.
- Santhanam, G., Ryu, S. I., Yu, B. M., Afshar, A., and Shenoy, K. V. (2006). A high-performance brain-computer interface. *Nature*, 442:195–198.
- Sayer, R. J., Friedlander, M. J., and Redman, S. J. (1990). The time course and amplitude of epsps evoked at synapses between pairs of CA3/CA1 neurons in the hippocampal slice. *J. Neurosci.*, 10:826–36.
- Segev, R., Goodhouse, J., Puchalla, J., and Berry, M. (2004). Recording spikes from a large fraction of the ganglion cells in a retinal patch. *Nature Neuroscience*, 7:1154–1161.
- Shumway, R. and Stoffer, D. (2006). *Time Series Analysis and Its Applications*. Springer.
- Song, S., Sjostrom, P. J., Reigl, M., Nelson, S., and Chklovskii, D. B. (2005). Highly nonrandom features of synaptic connectivity in local cortical circuits. *PLoS Biology*, 3:e68.
- Stein, R. B., Weber, D. J., Aoyagi, Y., Prochazka, A., Wagenaar, J. B. M., Shoham, S., and Normann, R. A. (2004). Coding of position by simultaneously recorded sensory neurones in the cat dorsal root ganglion. *J Physiol (Lond)*, 560(3):883–896.
- Stevenson, I., Rebesco, J., Hatsopoulos, N., Haga, Z., Miller, L., and Koerding, K. (2008). Inferring network structure from spikes. *Statistical Analysis of Neural Data meeting*.
- Stevenson, I. H., Rebesco, J. M., Hatsopoulos, N. G., Haga, Z., Miller, L. E., and Kording, K. P. (2009). Bayesian inference of functional connectivity and network structure from spikes. *IEEE Trans. Neural Systems and Rehab.*, 17:203–13.
- Stosiek, C., Garaschuk, O., Holthoff, K., and Konnerth, A. (2003). In vivo two-photon calcium imaging of neuronal networks. *Proceedings of The National Academy Of Sciences Of The United States Of America*, 100(12):7319–7324.
- Szobota, S., Gorostiza, P., Del Bene, F., Wyart, C., Fortin, D. L., Kolstad, K. D., Tulyathan, O., Volgraf, M., Numano, R., Aaron, H. L., Scott, E. K., Kramer, R. H., Flannery, J.,

- Baier, H., Trauner, D., and Isacoff, E. Y. (2007). Remote control of neuronal activity with a light-gated glutamate receptor. *Neuron*, 54:535–545.
- Thompson, A., Girdlestone, D., and West, D. (1988). Voltage-dependent currents prolong single-axon postsynaptic potentials in layer III pyramidal neurons in rat neocortical slices. *J Neurophysiol*, 60:1896–1907.
- Tibshirani, R. (1996). Regression shrinkage and selection via the lasso. *Journal of the Royal Statistical Society. Series B*, 58:267–288.
- Tipping, M. (2001). Sparse Bayesian learning and the relevance vector machine. *Journal of Machine Learning Research*, 1:211–244.
- Truccolo, W., Eden, U., Fellows, M., Donoghue, J., and Brown, E. (2005). A point process framework for relating neural spiking activity to spiking history, neural ensemble and extrinsic covariate effects. *Journal of Neurophysiology*, 93:1074–1089.
- Tsien, R. Y. (1989). Fluorescent probes of cell signaling. *Ann. Rev. Neurosci.*, 12:227–253.
- Vakorin, V. A., Krakovska, O. A., and McIntosh, A. R. (2009). Confounding effects of indirect connections on causality estimation. *Journal of Neuroscience Methods*, In press.
- Vidne, M., Kulkarni, J., Ahmadian, Y., Pillow, J., Shlens, J., Chichilnisky, E., Simoncelli, E., and Paninski, L. (2009). Inferring functional connectivity in an ensemble of retinal ganglion cells sharing a common input. *COSYNE*.
- Vogels, T. and Abbott, L. F. (2005). Signal Propagation and Logic Gating in Networks of Integrate-and-Fire Neurons. *J. Neurosci.*, 25(46):10786–10795.
- Vogelstein, J., Babadi, B., Watson, B., Yuste, R., and Paninski, L. (2008). Fast nonnegative deconvolution via tridiagonal interior-point methods, applied to calcium fluorescence data. *Statistical analysis of neural data (SAND) conference*.
- Vogelstein, J., Watson, B., Packer, A., Jedynak, B., Yuste, R., and Paninski, L. (2009). Spike inference from calcium imaging using sequential monte carlo methods. *Biophysical Journal*, In press.
- Wallace, D., zum Alten Borgloh, S., Astori, S., Yang, Y., Bausen, M., Kugler, S., Palmer, A., Tsien, R., Sprengel, R., Kerr, J., Denk, W., and Hasan, M. (2008). Single-spike detection in vitro and in vivo with a genetic Ca²⁺ sensor. *Nature methods*, 5(9):797–804.
- Yaksi, E. and Friedrich, R. W. (2006). Reconstruction of firing rate changes across neuronal populations by temporally deconvolved Ca²⁺ imaging. *Nature Methods*, 3(5):377–383.
- Yasuda, R., Nimchinsky, E. A., Scheuss, V., Polgruto, T. A., Oertner, T. G., Sabatini, B. L., and Svoboda, K. (2004). Imaging calcium concentration dynamics in small neuronal compartments. *Sci STKE*, 219:p15.
- Yuste, R., Konnerth, A., Masters, B., et al. (2006). *Imaging in Neuroscience and Development, A Laboratory Manual*.

YURIY MISHCHENKO
DEPT. OF STATISTICS AND
CENTER FOR THEORETICAL NEUROSCIENCE
COLUMBIA UNIVERSITY
1255 AMSTERDAM AVE
NEW YORK, NY 10027
[USA](#)
E-MAIL: yuriy.mishchenko@gmail.com

JOSHUA VOGELSTEIN
JOHNS HOPKINS UNIVERSITY
3400 N. CHARLES ST.
BALTIMORE, MD, 21205
[USA](#)
E-MAIL: joshuav@jhu.edu

LIAM PANINSKI
DEPT. OF STATISTICS AND
CENTER FOR THEORETICAL NEUROSCIENCE
COLUMBIA UNIVERSITY
1255 AMSTERDAM AVE
NEW YORK, NY 10027
[USA](#)
E-MAIL: liam@stat.columbia.edu
URL: <http://www.stat.columbia.edu/~liam>